Turbulent entrainment across turbulent-nonturbulent interfaces in stably stratified mixing layers

T. Watanabe,[1,*] J. J. Riley,[2] and K. Nagata[1]
[1]*Department of Aerospace Engineering, Nagoya University, Nagoya 464-8603, Japan*
[2]*Department of Mechanical Engineering, University of Washington, Seattle, Washington 98195, USA*
(Received 21 March 2017; published 30 October 2017)

The entrainment process in stably stratified mixing layers is studied in relation to the turbulent-nonturbulent interface (TNTI) using direct numerical simulations. The statistics are calculated with the interface coordinate in an Eulerian frame as well as with the Lagrangian fluid particles entrained from the nonturbulent to the turbulent regions. The characteristics of entrainment change as the buoyancy Reynolds number Re_b decreases and the flow begins to layer. The baroclinic torque delays the enstrophy growth of the entrained fluids at small Re_b, while this effect is less efficient for large Re_b. The entrained particle movement within the TNTI layer is dominated by the small dissipative scales, and the rapid decay of the kinetic energy dissipation rate due to buoyancy causes the entrained particle movement relative to the interface location to become slower. Although the Eulerian statistics confirm that there exists turbulent fluid with strong vorticity or with large buoyancy frequency near the TNTI, the entrained fluid particles circumvent these regions by passing through the TNTI in strain-dominant regions or in regions with small buoyancy frequency. The multiparticle statistics show that once the nonturbulent fluid volumes are entrained, they are deformed into flattened shapes in the vertical direction and diffuse in the horizontal direction. When Re_b is large enough for small-scale turbulence to exist, the entrained fluid is able to penetrate into the turbulent core region. Once the flow begins to layer with decreasing Re_b, however, the entrained fluid volume remains near the outer edge of the turbulent region and forms a stably stratified layer without vertical overturning.

DOI: 10.1103/PhysRevFluids.2.104803

I. INTRODUCTION

Localized turbulent regions often appear in the natural environment surrounded by nonturbulent or weakly turbulent fluids. Examples are the atmospheric boundary layer [1] and the ocean mixed layer [2], where the turbulent fluids are separated from the external regions by a thin interfacial layer, across which the flow characteristics change significantly. In the case that the outside fluid is nonturbulent (irrotational), this interfacial layer is called the turbulent-nonturbulent interface (TNTI) [3], which also exists in various canonical flows, such as mixing layers, jets, and boundary layers. Corrsin and Kistler [4] predicted that the vorticity diffusion within the TNTI layer causes the spatial development of turbulent flows, resulting in the entrainment of nonturbulent fluid. Furthermore, this interfacial region is responsible for the exchanges of mass, energy, momentum, and scalars between the turbulent and the nonturbulent flows. Thus, the flow dynamics near the TNTI layer, as well as associated phenomena such as scalar mixing, are crucial in the behavior of environmental flows [1,5]. For example, the entrainment rate of turbulence often governs the flow evolution in environmental flows [6].

Observations in the atmosphere and oceans have shown that flows are often strongly stably stratified [2,7,8]. However, most studies of TNTIs, defined in terms of vorticity rather than density [9,10], are limited to nonstratified flows. As proposed by Corrsin and Kistler [4], a very thin layer, so called "viscous superlayer," where the fluid acquires vorticity by viscous diffusion, has

*watanabe.tomoaki@c.nagoya-u.jp

been found at the edge of the turbulence in both direct numerical simulations [11] and in laboratory experiments [12,13]. Furthermore, an adjacent layer called the "turbulent sublayer" was also found between the viscous superlayer and the turbulent region [14]. The relationship between entrainment and the TNTI has been studied in nonstratified flows. The outer edge of the interface layer propagates into the nonturbulent fluid, resulting in the entrainment of fluid [13]. This propagation velocity was found to be dominated by viscous effects and to scale with the Kolmogorov velocity [14,15] and is related to the global development of turbulent flows through the surface area of the outer edge of the interface layer. Furthermore, the Lagrangian tracking of the entrained fluid showed that the entrained fluid motion is dominated by different processes depending on the location within the TNTI layer: by viscous effects in the viscous superlayer and by inviscid small-scale turbulent motions in the turbulent sublayer [16]. During the entrainment of the fluid, the physical processes dominating the enstrophy and rate-of-strain change depending on the fluid location [17]. Chauhan *et al.* [18] also showed, from the movement of the TNTI detected with the isosurface of local turbulent kinetic energy, that the entrainment velocity is characterized by two distinctive length scales.

The importance of the interface separating two different fluids in stratified flows has been recognized, and therefore the density interface has been studied in experiments [9,10,19–21], with numerical simulations [22], and with theoretical approaches [23,24]. The TNTI defined in terms of vorticity, in particular, rather than an advective-diffusive scalar field, such as density, has been studied in detail recently using high resolution direct numerical simulations [25] and two- and three-dimensional velocity measurements in experiments [15]. The interfaces defined with vorticity or with a scalar are different especially when the Schmidt (Prandtl) number Sc (Pr) is not unity [26]. This is because a nonturbulent fluid gains a scalar by molecular diffusion and vorticity by viscous diffusion [27], where the diffusion coefficients are equal in the case of $\mathrm{Sc} = 1$ ($\mathrm{Pr} = 1$). The statistical properties of the TNTI have been revealed from statistics calculated using the local interface coordinate, whose origin is located at the TNTI [28]. Several studies based on the statistics in relation to the TNTI have been carried out in stratified flows [29–33]. In gravity currents, Krug *et al.* [29] experimentally investigated the TNTI, and showed that the entrainment rate is reduced by the stratification because of the reduction of the TNTI surface area. DNS of a stratified wake showed that, when the flow outside the turbulent fluid is stably stratified, the turbulent region near the TNTI is strongly affected by the emission of internal gravity waves, which transfer kinetic energy from the turbulent fluid [30]. We have also studied the effects of stable stratification on the small-scale dynamics near the TNTI using the DNS of stratified mixing layers [31].

In this paper, we investigate the entrainment process across the TNTI in stably stratified mixing layers [34]. We perform DNS of temporally evolving stratified mixing layers, where the Kelvin-Helmholtz (KH) instability generates three-dimensional turbulence. This process of turbulence generation is sometimes considered a good model for turbulence generation in geophysical flows [35,36]. The flow is considered with density stratification localized within the shear layer, and, therefore, the density is uniform outside the mixing layer; so the ambient fluid does not allow the propagation of internal gravity waves, unlike cases where the external region is stably stratified [37]. In this flow, the flow structure significantly changes with time [38]. In the initial state, three-dimensional small-scale turbulence is generated by the KH instability. Initially, buoyancy suppresses the large-scale turbulent motion, and, as the flow evolves, the fluid motions from large to smaller scales begin to be strongly affected by buoyancy, forming layered structures. In our recent study [31], we have presented the statistics near the TNTI in the stratified mixing layer at the early stage of the flow development, where the buoyancy Reynolds number is high enough for the small-scale, three-dimensional turbulence to exist. In this paper, we investigate the entrainment process for the different stages of the flow development, including the later times at which the flow begins to become layered. Previous studies of the TNTI have shown that the small scale characteristics are important in phenomena associated with the TNTI, such as the entrainment mechanism [3]. The influence of stable stratification on the small scales is often discussed in terms of the buoyancy Reynolds number, $\mathrm{Re}_b = (\tilde{\varepsilon}/\tilde{N}^3)$, where $\tilde{\varepsilon}$ is the kinetic energy dissipation rate and $\tilde{N}$ the buoyancy frequency [39]. This quantity can be defined in terms of the ratio of the largest length scale which

can overturn, the Ozmidov scale, to the smallest length scale of turbulence, the Kolmogorov scale. For Re_b large enough, there is a range of energetic scales of turbulence which can act to entrain nonturbulent fluid. As Re_b becomes small, however, even the smaller-scale motions become affected by the stable stratification. Therefore, Re_b is a key parameter in the entrainment process across the TNTI layer, although other parameters are also used in parametrizations of mixing efficiency in stably stratified flows [40].

Lagrangian tracking of fluid particles being entrained is useful for studying the entrainment process, and the Lagrangian statistics during entrainment have been reported in nonstratified flows [15–17,41,42]. We apply these methods to stratified mixing layers. The Lagrangian statistics only contain the contribution of the fluid being entrained, while the Eulerian statistics are studied for both entrained fluids and for fluids existing in the turbulent region. We compare the Lagrangian statistics with their Eulerian counterparts to highlight the entrainment characteristics. For this purpose, the entrained fluid particle locations are examined in relation to the TNTI location by tracking the TNTI movement. This allows us to link the Lagrangian statistics to the layered structure of the TNTI [16] and to investigate how deeply the entrained particles are able to penetrate across the TNTI into the turbulent core region. Furthermore, we also discuss the relationship between the entrainment and the flow structures using multiparticle statistics, which are related to the deformation of material volumes [42].

The new DNS of the stratified mixing layer are described in Sec. II. The Eulerian statistics including the temporal evolution of the statistics and the conditional statistics near the TNTI are presented in Sec. III. The Lagrangian statistics for the entrained particles are discussed in Sec. IV. Finally, Sec. V summarizes the conclusions.

II. DIRECT NUMERICAL SIMULATION OF STRATIFIED MIXING LAYER

Temporally evolving mixing layers in a stably stratified environment [39,43,44] are computed by the DNS of the Navier-Stokes equations within the Boussinesq approximation. The streamwise, spanwise, and vertical directions are represented by x, y, and z, respectively. The flow develops with time from an initial field described by a characteristic density of the fluid ρ_0, the velocity and density jumps across the mixing layer (ΔU and $\Delta\rho$, respectively), and the initial layer thickness h_0. The nondimensional variables are then introduced as

$$x_i = \frac{\tilde{x}_i}{h_0}, \quad t = \frac{\tilde{t}_i}{h_0/\Delta U}, \quad u_i = \frac{\tilde{u}_i}{\Delta U}, \quad \rho = \frac{\tilde{\rho}}{\Delta\rho}, \quad p = \frac{\tilde{p}}{\rho_0 \Delta U^2}, \tag{1}$$

where x_i, t, u_i, ρ, and p denote position, time, velocity, density, and pressure, respectively, and the tilde represents the dimensional variables. The initial nondimensional velocity and density fields are given by

$$u(x,y,z) = \tfrac{1}{2}\tanh(2z) + u'(x,y,z), \tag{2}$$

$$v(x,y,z) = v'(x,y,z), \tag{3}$$

$$w(x,y,z) = w'(x,y,z), \tag{4}$$

$$\rho(x,y,z) = \rho_0/\Delta\rho - \tfrac{1}{2}\tanh(2z), \tag{5}$$

where u', v', w' are the initial velocity fluctuations, which have nonzero values within $|z| < 0.7$, and are generated by a diffusion process [45] with the characteristic lengthscale $0.25h_0$ and root mean square (rms) velocity fluctuations $0.01\Delta U$.

The governing equations are the continuity equation, the momentum equation, and transport equation for the density ρ, which are written in nondimensional form as follows:

$$\frac{\partial u_i}{\partial x_i} = 0, \tag{6}$$

$$\frac{\partial u_i}{\partial t} + \frac{\partial u_i u_j}{\partial x_j} = -\frac{\partial p}{\partial x_i} + \frac{1}{\mathrm{Re}}\frac{\partial^2 u_i}{\partial x_j \partial x_j} - Ri\rho'\delta_{i3}, \tag{7}$$

$$\frac{\partial \rho}{\partial t} + \frac{\partial u_j \rho}{\partial x_j} = \frac{1}{\mathrm{RePr}}\frac{\partial^2 \rho}{\partial x_j \partial x_j}, \tag{8}$$

where $\rho' = \rho - \rho_0/\Delta\rho$. The nondimensional parameters in these equations are the Reynolds number $\mathrm{Re} = \Delta U h_0/\nu$, the Prandtl number $\mathrm{Pr} = \nu/\kappa$, and the Richardson number $\mathrm{Ri} = g\Delta\rho h_0/\rho_0 \Delta U_0^2$, where ν is the kinematic viscosity, κ is the diffusivity coefficient for density, and g is the gravitational acceleration. We consider the stably stratified mixing layer for three cases determined by three sets of parameters, i.e., (Re, Ri, Pr) = (2000, 0.06, 1), (2000, 0.08, 1), and (1200, 0.06, 1), which are referred to as Re20Ri06, Re20Ri08, and Re12Ri06, respectively. We discuss the temporal development of statistics mainly for case Re20Ri06, since most results are qualitatively similar in all three DNS cases. The computational domain is periodic in the horizontal (x and y) directions, while for the vertical (z) direction, the impermeability condition is used for the vertical velocity and zero-flux conditions are used for the horizontal velocity and density following Smyth [39].

The size of the computational domain normalized by h_0 is $L_x \times L_y \times L_z = 48 \times 28 \times 80$, and the number of computational grid points is $N_x \times N_y \times N_z = 1200 \times 800 \times 1500$. There is fixed grid spacing in the horizontal directions while the grid is stretched in the vertical direction near the vertical boundaries. The DNS is performed with the same code as in our previous study [31]. For completeness, we briefly present the numerical methods. The DNS code is based on a fractional step method with fully conservative finite-difference schemes [46] for spatial discretization and a third-order Runge-Kutta method for temporal advancement with a constant time increment $\Delta t = 0.01$. A fourth-order scheme and a second-order scheme are used for the spatial discretization in the horizontal directions and vertical direction, respectively. The Bi-CGSTAB method is used for solving the Poisson equation for pressure [47].

The statistics are computed from snapshots by taking an average, denoted by $\langle\ \rangle$, in the homogeneous (x and y) directions. The DNS is performed until $t = 320$, by which time the centerline buoyancy Reynolds number has decreased to less than $O(10)$, indicating that turbulence at all length scales is strongly influenced by buoyancy. The main results presented in this paper are taken from $t \geqslant 130$, for which the computational grid spacing is smaller than 1.5η on the centerline in the all DNS, where $\tilde{\eta} = (\nu^3/\langle\tilde{\varepsilon}\rangle)^{1/4}$ is the Kolmogorov lengthscale and $\langle\tilde{\varepsilon}\rangle$ is the mean kinetic energy dissipation rate $\langle\tilde{\varepsilon}\rangle = 2\nu\langle\tilde{S}_{ij}\tilde{S}_{ij}\rangle$ ($\tilde{S}_{ij}$: rate of strain tensor).

III. EULERIAN STATISTICS OF A STRATIFIED MIXING LAYER

A. Temporal evolution

The fundamental characteristics of the flow are presented here before we discuss the entrainment in the stratified mixing layer. Figure 1(a) shows the thickness of the mixing layer defined from the mean velocity and density profiles as

$$\delta_U = \int_{-L_z/2}^{L_z/2} (u_1 - \langle u\rangle)(\langle u\rangle - u_2)dz, \tag{9}$$

$$\delta_\rho = \int_{-L_z/2}^{L_z/2} (\rho_1' - \langle\rho'\rangle)(\langle\rho'\rangle - \rho_2')dz, \tag{10}$$

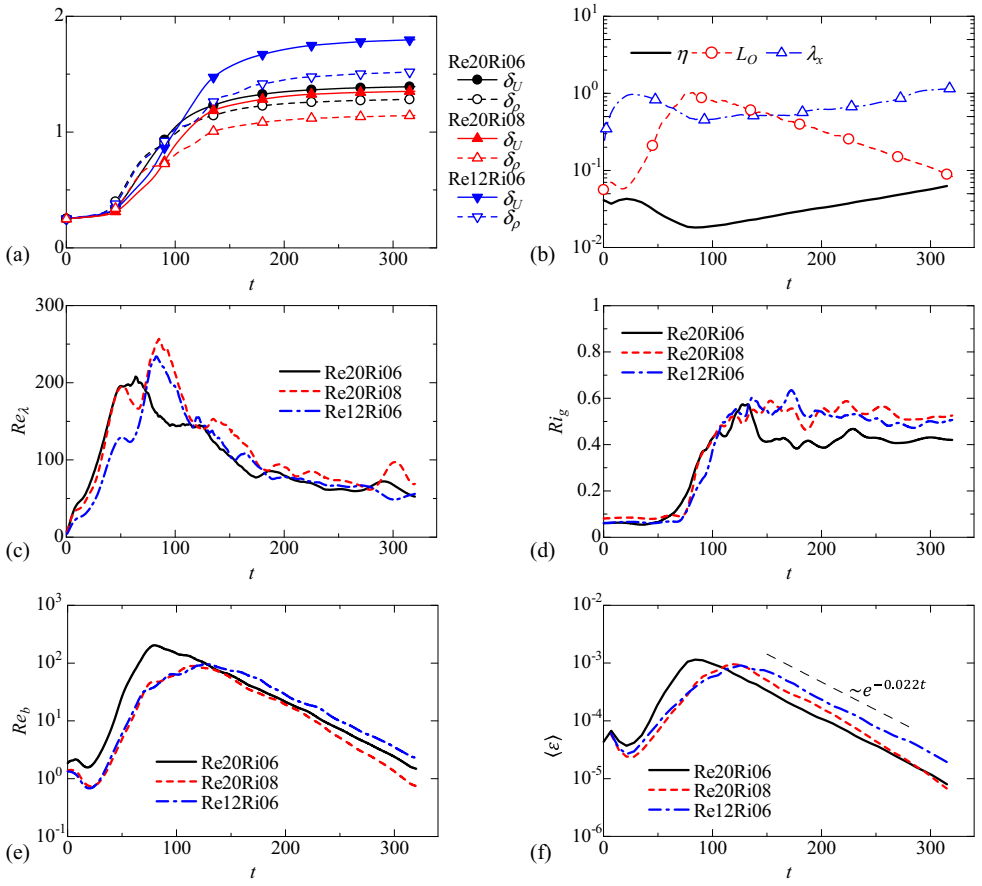

FIG. 1. Temporal evolution of the stratified mixing layer. (a) The thicknesses of the stratified mixing layer δ_U and δ_ρ. (b) Kolmogorov scale η, Ozmidov scale L_O, and Taylor microscale λ_x calculated from streamwise velocity on the centerline ($z = 0$) for case Re20Ri06. (c) Turbulent Reynolds number Re_λ, (d) gradient Richardson number Ri_g, (e) buoyancy Reynolds number Re_b, and (f) mean kinetic energy dissipation rate on the centerline.

where the subscripts 1 and 2 refer to the mean values at $z = L_z/2$ and $-L_z/2$, respectively. The layer thickness rapidly grows in its initial stage, and then the growth rate is suppressed at a later time as observed in previous DNS of stratified mixing layers [34]. The thicknesses δ_U and δ_ρ are larger in the lower Re case, Re12Ri06, which can be related to stronger viscous (molecular) diffusive effects on the mean velocity and density profiles for lower Re. A similar Re dependence can be also found in the shear layer thickness normalized by h_0 in previous DNS [34]. Figure 1(b) shows the centerline evolution of the Kolmogorov lengthscale η, the Ozmidov scale $L_O = (\langle\varepsilon\rangle/N^3)^{1/2}$, and Taylor microscale defined with the streamwise velocity $\lambda_x = \sqrt{\langle u'^2\rangle/\langle(\partial u'/\partial x)^2\rangle}$ ($u' = u - \langle u\rangle$ is the streamwise velocity fluctuation) in Re20Ri06, where the buoyancy frequency $\tilde{N}$ is given by $\tilde{N} = \sqrt{-(g/\rho_0)\langle\partial\tilde{\rho}/\partial\tilde{z}\rangle}$, and $N = \tilde{N}h_0/\Delta U$. The temporal development of these length scales agrees well with previous DNS studies [34]. At the initial stage of decay, the small scales are less affected by the buoyancy than the large scales, as evidenced from L_O being much larger than η. After the growth rate of the mixing layer has substantially decreased, however, L_O decreases with time while λ_x and η increase, and ultimately buoyancy becomes important even at the small dissipative-scales.

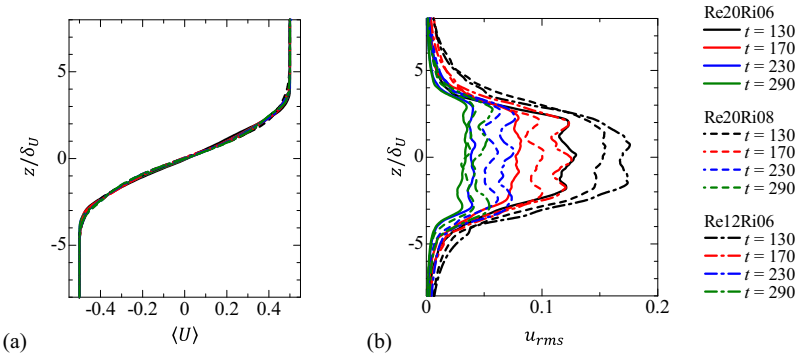

FIG. 2. Vertical profiles of (a) mean streamwise velocity $\langle u \rangle$ and (b) rms value of streamwise velocity fluctuation $u_{\rm rms} = \langle u'^2 \rangle^{1/2}$. The vertical coordinate is normalized by δ_U.

The temporal evolutions of the centerline values of the three nondimensional parameters are shown in Figs. 1(c)–1(e); the parameters are: the turbulent Reynolds number Re_λ, the buoyancy Reynolds number Re_b, and the gradient Richardson number, defined by

$$\mathrm{Re}_\lambda = \frac{\langle \tilde{u}'^2 \rangle^{1/2} \tilde{\lambda}_x}{\nu}, \quad \mathrm{Re}_b = \left(\frac{\tilde{L}_O}{\tilde{\eta}} \right)^{4/3} = \frac{\langle \tilde{\varepsilon} \rangle}{\nu \tilde{N}^2}, \quad \mathrm{Ri}_g = -\frac{g \langle \partial \tilde{\rho} / \partial \tilde{z} \rangle}{\rho_0 \langle \partial \tilde{u} / \partial \tilde{z} \rangle^2}, \tag{11}$$

where the total density gradient is used in Eq. (11).

During the decay period Re_λ decreases from $\mathrm{Re}_\lambda \approx 200$ to 50, and $\mathrm{Ri}_g \approx 0.4$–$0.5$, almost independent of time. On the other hand, Re_b keeps decreasing from the maximum value Re_b greater than 100 toward $O(1)$, at which point both the small-scale and the large-scale turbulent motions are being damped by the buoyancy. Time independence of Ri_g, which was also found in DNS by Brucker and Sarkar [44], indicates that the turbulent region remains in a marginal state of instability, which is related to a asymptotic behavior of the thickness of the shear layer measured by mean density and velocity profiles. At the initial stage of the decay, Re_b is larger than $O(100)$ and the small-scale turbulence dynamics on the centerline is somewhat free from the direct influence of the stratification [39]. Figure 1(f) shows the decay of the mean kinetic energy dissipation rate, $\langle \varepsilon \rangle$, on the centerline, which can be related to the mixing efficiency in stratified flows [48]. The mean kinetic energy dissipation rate exhibits an exponential decay, which is more rapid than in nonstratified mixing layers [42], implying that the buoyancy suppresses the mixing in the stratified mixing layer.

Figure 2 shows the vertical profiles of mean streamwise velocity $\langle u \rangle$ and rms value of streamwise velocity fluctuation $u_{\rm rms}$. The profile of $\langle u \rangle$ collapses well while $u_{\rm rms}$ continually decreases with time, unlike in nonstratified mixing layers where $u_{\rm rms}$ hardly changes with time in a self-similar regime. This decrease with time was explained by the suppression of turbulence production due to the significant reduction of Reynolds shear stress $\langle u'w' \rangle$ by buoyancy effects [44].

Visualization of ρ' in Fig. 3 also confirms the dependence on Re_b of the different stages of the decay of the stratified mixing layer. One can easily see density fluctuations associated with small-scale turbulence at earlier times with large Re_b, while these are missing in later times for which $\mathrm{Re}_b < 30$; finally, the flow starts to become layered for $t \geqslant 230$.

B. Conditional statistics near TNTIs

The entrainment in the stratified mixing layer is studied in relation to the TNTI. The interface is detected by defining its location at the isosurface of the vorticity magnitude $|\boldsymbol{\omega}| = \omega_{\rm th}$, where the threshold $\omega_{\rm th}$ is determined from the $\omega_{\rm th}$-dependence of the turbulent volume, as in previous studies of the TNTI [26,41,49]. We set $\omega_{\rm th} = 0.04 \langle |\boldsymbol{\omega}| \rangle$, where $\langle |\boldsymbol{\omega}| \rangle$ is on the centerline. The same threshold

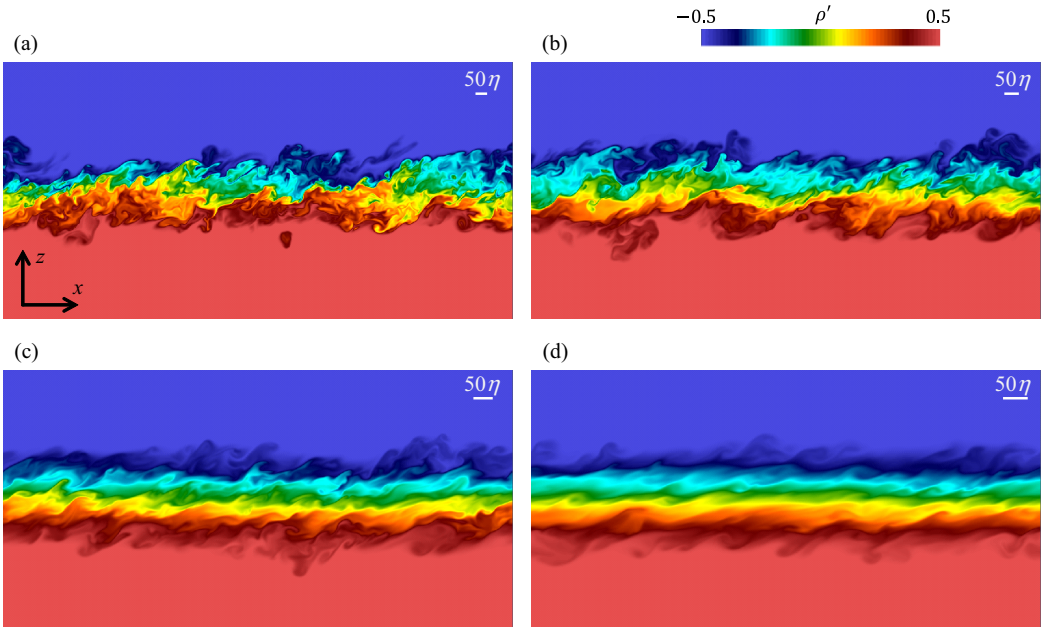

FIG. 3. Visualization of density field ρ' on an x-z plane at (a) $t = 130$ ($\mathrm{Re}_b = 90$), (b) $t = 170$ ($\mathrm{Re}_b = 39$), (c) $t = 230$ ($\mathrm{Re}_b = 11$), and (d) $t = 290$ ($\mathrm{Re}_b = 3$), where Re_b is calculated on the centerline. The total extent of the computational domain in the vertical (z) dimension is not shown in the figure.

was used in our recent DNS of stratified mixing layers [31]. The isosurface $|\boldsymbol{\omega}| = \omega_{\mathrm{th}}$ is chosen so that it is located near the outer edge of the TNTI layer, and this isosurface is referred to as the irrotational boundary [26]. To clarify the discussion of the TNTI region, we employ the following terminology: the isosurface defined by $|\boldsymbol{\omega}| = \omega_{\mathrm{th}}$ is called the irrotational boundary, whereas the region just inside this isosurface characterized by a large gradient in $|\boldsymbol{\omega}|$ is called the TNTI layer. We also refer to the region with $|\boldsymbol{\omega}| > \omega_{\mathrm{th}}$ to as the turbulent region. Furthermore, "turbulent core region" is used for the turbulent region inside the TNTI layer where the mean vorticity magnitude is almost uniform [14].

The statistics are calculated conditioned on a distance from the irrotational boundary, ζ_I, whose direction is given by the enstrophy gradient $-\nabla\omega^2$, where positive ζ_I is in the nonturbulent region. The average based upon the interface coordinate is denoted by $\langle\ \rangle_I$. The statistics are calculated for the upper TNTI. Because the flow is antisymmetric, the lower interface is also used for calculating conditional statistics by changing the sign of relevant variables. We present the conditional statistics as a function of ζ_I/η, where the value of η is taken at the centerline. It should be noted that the stratification is localized in the mixing layer and internal gravity waves are absent in nonturbulent regions, and therefore vorticity rather than potential vorticity can be used for detecting the turbulent region [30].

Figure 4(a) shows the conditional mean vorticity magnitude as a function of ζ_I/η at $t = 130$, 170, 230, and 290. The vorticity magnitude decreases sharply near and across the TNTI layer. Figure 4(b) shows the conditional mean kinetic energy dissipation rate $\langle\varepsilon\rangle_I$, which also greatly changes across the TNTI layer. It should be noted that the magnitude of $\langle\varepsilon\rangle_I$ in the vicinity of the TNTI layer ($\zeta_I \approx -15\eta$) is very similar to that deep inside of the turbulent core region ($\zeta_I \approx -50\eta$). Thus, buoyancy causes the rapid temporal decay of ε in the turbulent core region near the TNTI ($\zeta_I \approx -15\eta$) as well as on the centerline [Fig. 1(f)].

The thickness of the TNTI layer is estimated with $\omega_I' = d\langle|\boldsymbol{\omega}|\rangle_I/d\zeta_I$, an example of which is shown in Fig. 5(a). Because of a large difference in vorticity between the turbulent and nonturbulent

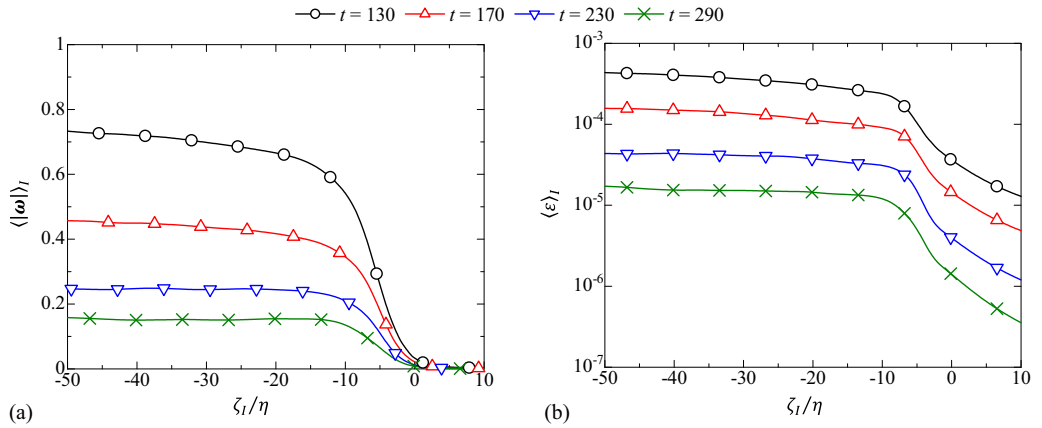

FIG. 4. Temporal variations of conditional average of (a) vorticity magnitude and (b) kinetic energy dissipation rate near the TNTI.

fluids, $-\omega_I'$ has a large peak within the TNTI layer. The thickness of the TNTI, δ_I, is estimated with the location where $-\omega_I'$ is equal to 25% of its maximum $[-\omega_I']_{\max}$ as defined in Fig. 5(a). Figure 5(b) shows the temporal variation of δ_I, which increases with time. However, the thickness normalized by the Kolmogorov scale, δ_I/η, hardly changes with time as seen in Fig. 5(c), and the average of δ_I/η taken at 4 different times in all DNS is 12η, which is close to the value for nonstratified turbulent flows [26], although the structure of the stratified mixing layer changes with time as shown in Fig. 3. It has been shown that the viscous superlayer with the thickness $\sim 4\eta$, where the vorticity evolution is dominated by the viscous effects, is formed at outer edge of the TNTI layer in the stratified mixing layer [31]. Thus, we can identify the region $-4\eta \leqslant \zeta_I \leqslant 0$ as the viscous superlayer while the turbulent sublayer can be found for $-12\eta \leqslant \zeta_I \leqslant -4\eta$.

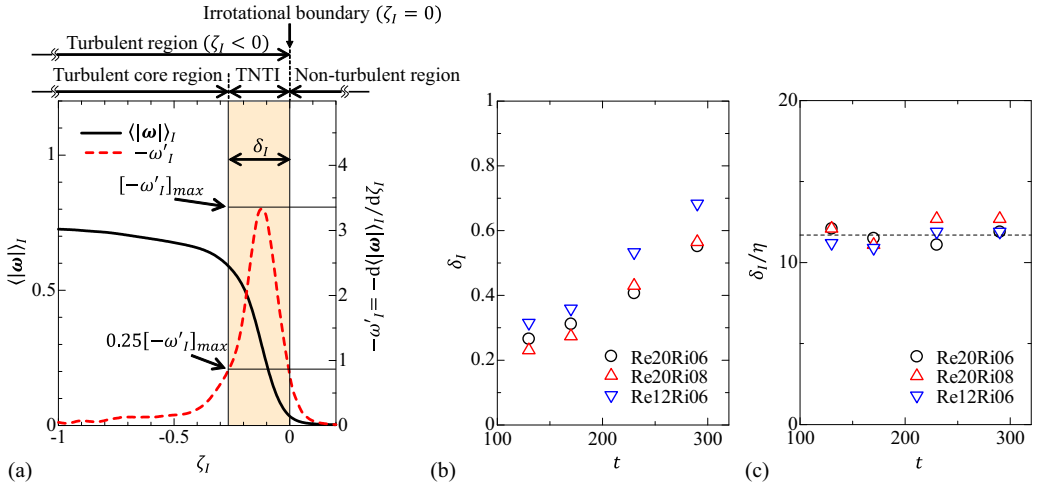

FIG. 5. (a) Estimation of the thickness of the TNTI layer, δ_I, based on the conditional mean vorticity. $\langle|\boldsymbol{\omega}|\rangle_I$ and $-\omega_I' = -d\langle|\boldsymbol{\omega}|\rangle_I/d\zeta_I$ are shown for $t = 130$ in Re20Ri06. δ_I is estimated with the location where $-\omega_I'$ reaches 25% of the maximum $[-\omega_I']_{\max}$. Temporal variation of (b) δ_I and (c) δ_I/η, where η is taken from the centerline. The horizontal broken line ($\delta_I = 12\eta$) in (c) indicates the average value of δ_I/η.

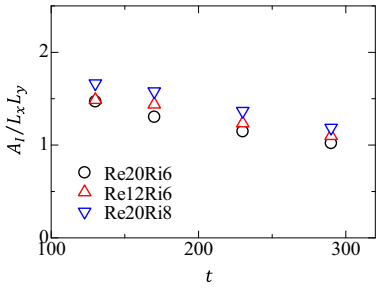

FIG. 6. Surface area of irrotational boundary A divided by a horizontal area of the computational box L_xL_y.

The propagation velocity of the irrotational boundary is related to the total entrainment rate through its surface area A. Figure 6 shows the temporal evolution of A divided by a horizontal area of the computational box L_xL_y, computed with the surface integration tool in ParaView following Jahanbakhshi and Madnia [50]. Values of A/L_xL_y in the stratified shear layers are smaller than $A/L_xL_y \approx 7.3$ found in nonstratified mixing layer (at convective Mach number 0.2) [50]. The surface area continually decreases with time, as seen in Fig. 6, which can be related to the slower growth rate of the shear layer thickness found in Fig. 1(a) at later times. The reduction of the surface area by buoyancy was also reported in a study of gravity currents [29].

We can define the local mean vertical shear near the TNTI as $\tilde{S}_I = \langle \partial\tilde{u}/\partial\tilde{z}\rangle_I$. Similarly, the local buoyancy frequency can be defined with the conditional average as $\tilde{N}_I = \sqrt{-(g/\rho_0)\langle \partial\tilde{\rho}/\partial\tilde{z}\rangle_I}$. Figures 7(a) and 7(b) show S_I and N_I, both of which increase across the TNTI layer from the nonturbulent toward the turbulent regions. Both S_I and N_I decrease with time near the TNTI layer. Figures 7(c) and 7(d) show the local Richardson number $\mathrm{Ri}_I = N_I^2/S_I^2$ and the local buoyancy Reynolds number $\mathrm{Re}_{bI} = \langle\tilde{\varepsilon}\rangle_I/\nu\tilde{N}_I^2$, respectively. In the turbulent region, except within the TNTI layer, Ri_I mainly increases from $t = 170$ to 230, during which Re_{bI} decreases from 100 to 20. These changes of Ri_I and Re_{bI} are consistent with the visualization of density in Fig. 3 where, during the period $t = 170$ to 230, the flow structures change from being more turbulent-like, to becoming layered without significant small-scale fluctuations. The decrease in Re_{bI} with time is related to the rapid temporal decay of $\langle\varepsilon\rangle_I$; the local minimum value of Re_{bI} in the TNTI layer, at $\zeta_I \approx -4\eta$, could be due to the increase in Ri_I to above 1 in the TNTI layer, possibly acting to stabilize the turbulence in that region. The Richardson number for $-10 \leqslant \zeta/\eta \leqslant 0$ hardly changes with time, implying that the time scale ratio between the shear $1/S_I$ and the buoyancy $1/N_I$ is almost independent of time. This observation of the time-independent Ri_I agrees with the TNTI in gravity currents, for which a detailed analysis has been presented for the evolution of vertical gradients of density and velocity [29].

The vertical overturning motions in density stratified flows can be observed from the isopycnals, whose unit normal is given by $\boldsymbol{n}_\rho = \nabla\rho/|\nabla\rho|$. The vertical component of $\boldsymbol{n}_\rho$, denoted by $n_{\rho z} = \boldsymbol{n}_\rho \cdot \boldsymbol{e}_z$, is the cosine of the angle between the vertical direction and the density gradient. For a stably stratified state without the density fluctuations, $n_{\rho z}$ is equal to -1, while fluids with overturning motions have positive $n_{\rho z}$. Figure 8 shows plots of the probability density function (PDF) of $n_{\rho z}$ near the TNTI, which have large peaks at $n_{\rho z} = -1$. The peaks at $t = 130$ decrease as ζ_I/η goes from -2 toward -18. In addition, the probability for positive $n_{\rho z}$ becomes large in the turbulent region, except within the TNTI layer, as confirmed from the PDF at $\zeta_I/\eta = -18$. Thus, overturns occur more frequently in the turbulent core region than within the TNTI layer. This can be related to the small buoyancy Reynolds number within the TNTI, which results from the suppression of small-scale turbulent motions. As t increases, the probability for $n_{\rho z} = -1$ also increases, and the vertical overturning motions become less and less frequent for flows within the TNTI layer ($-12\eta \leqslant \zeta_I \leqslant 0$), as evidenced by the increasingly lower probability for $n_{\rho z} > 0$. However, in the turbulent core region at $\zeta_I/\eta = -18$, the probability for $n_{\rho z} > 0$ is still nonzero and overturns can

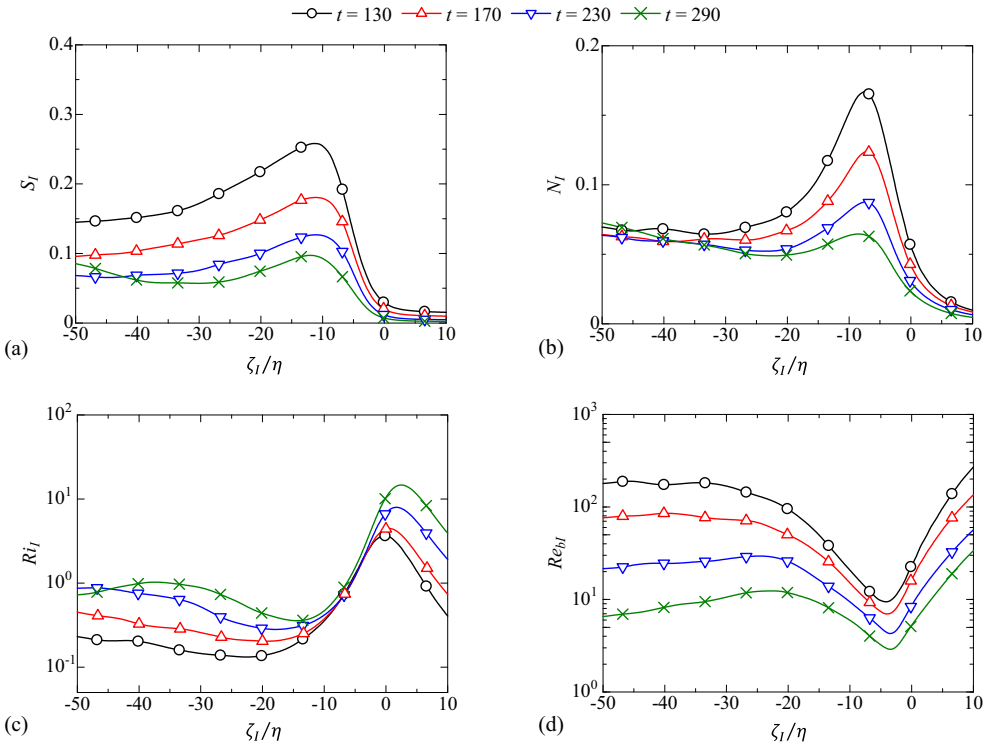

FIG. 7. Characteristics of stratified mixing layer near the TNTI in Re20Ri06. (a) Vertical shear S_I ($\tilde{S}_I = \langle \partial\tilde{u}/\partial\tilde{z}\rangle_I$). (b) Buoyancy frequency N_I ($\tilde{N}_I = \sqrt{-(g/\rho_0)\langle\partial\tilde{\rho}/\partial\tilde{z}\rangle_I}$). (c) Local Richardson number $\mathrm{Ri}_I = N_I^2/S_I^2$. (*d*) Buoyancy Reynolds number $\mathrm{Re}_{bI} = \langle\tilde{\varepsilon}\rangle_I/\nu\tilde{N}_I^2$.

be found in some parts of stratified mixing layer, even after the buoyancy Reynolds number reaches below 10 ($t = 290$).

Since turbulence is regarded as motion with nonzero vorticity, the entrainment of nonturbulent fluid has been examined by studying the vorticity evolution near the TNTI [3]. The equation for

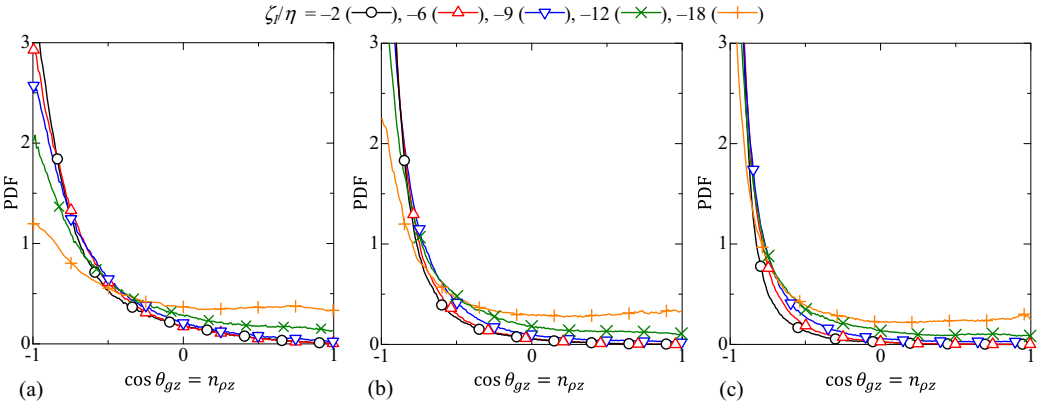

FIG. 8. PDFs of the vertical component of normalized density gradient $n_{\rho z} = \boldsymbol{n}_\rho \cdot \boldsymbol{e}_z$ near the TNTI at (a) $t = 130$, (b) $t = 230$, and (c) $t = 290$ in Re20Ri06, where $n_{\rho z}$ represents the cosine of the angle between the vertical direction and the density gradient direction θ_{gz}.

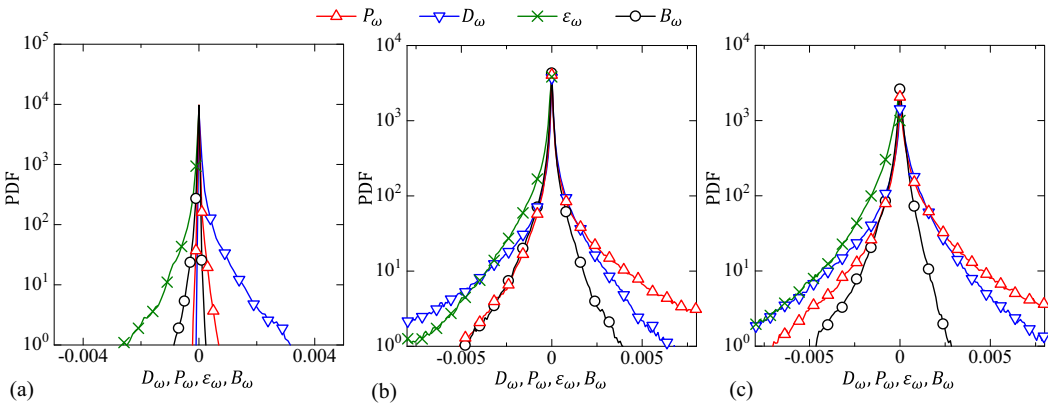

FIG. 9. Enstrophy evolution near the TNTI at $t = 290$ in Re20Ri06. PDFs of viscous diffusion term D_ω, production term P_ω, viscous dissipation term ε_ω, and baroclinic torque B_ω at (a) $\zeta_I/\eta = -2$, (b) $\zeta_I/\eta = -9$, and (c) $\zeta_I/\eta = -18$.

enstrophy $\omega^2/2$ within the Boussinesq approximation is given by

$$\frac{D\omega^2/2}{Dt} = \omega_i S_{ij} \omega_j + \frac{1}{\mathrm{Re}} \nabla^2(\omega^2/2) - \frac{1}{\mathrm{Re}} \nabla \omega_i \cdot \nabla \omega_i + \mathrm{Ri} \varepsilon_{ij3} \omega_i \frac{\partial \rho}{\partial x_j}, \tag{12}$$

where, on the right-hand side, the first term is the production, or vortex stretching/compression, term P_ω, the second term is the viscous diffusion term D_ω, the third term is the viscous dissipation rate term ε_ω, and the last term is the baroclinic torque B_ω. It has been shown that, in stratified mixing layers with high Re_b in the turbulent core region, the statistics of Eq. (12) near the TNTI behave in a qualitatively similar manner to those for nonstratified flows except for the baroclinic torque B_ω, which reduces the enstrophy near the TNTI [31]. Figure 9 shows the PDF of each term in Eq. (12) near the TNTI at $t = 290$, at which point in time Re_b on the centerline is small enough for turbulent motions at small scales to be strongly influenced by stratification. At $\zeta_I/\eta = -2$, the viscous terms D_ω and ε_ω are dominant over the production and baroclinic torque terms, and the vorticity region growth is caused by the viscous diffusion, as in the viscous superlayer in nonstratified flows [11]. The production and baroclinic torque terms become important at $\zeta_I/\eta = -9$ and -18, which are located within the turbulent sublayer and in the turbulent core region, respectively. The PDF of P_ω is positively skewed, as vortex stretching is dominant over vortex compression, as in nonstratified flows. However, even at $\zeta_I/\eta = -18$, the local change in ω^2 due to D_ω is comparable to that due to P_ω, although P_ω in nonstratified flows and stratified flows with large Re_b has a larger contribution to the local enstrophy growth than the viscous diffusion term [31,49]. This might be explained by the misalignment between the vorticity and the extensive strain caused by buoyancy observed in a low Re_b regime [39], which was also found near the TNTI [31].

IV. LAGRANGIAN STATISTICS DURING THE ENTRAINMENT

A. Lagrangian analysis of the entrainment

Lagrangian properties of the entrainment are studied by tracking fluid particles, following previous DNS studies of nonstratified mixing layers [16,42]. We consider tetrahedra, each consisting of four fluid particles, which have been used for studying the evolution of material volume in turbulent flows [51]. At a chosen time t_0 of the simulation, 40 000 tetrahedra are seeded in the nonturbulent regions near the TNTI. The initial location of the one of four particles of a tetrahedron, $\boldsymbol{x}_1 = \boldsymbol{x}_0$, is randomly determined to be in the nonturbulent region within 3η from the irrotational boundary detected with the threshold $\omega_{th} = 0.04\langle|\boldsymbol{\omega}|\rangle$ at t_0. Then, following Schumacher [52], the other

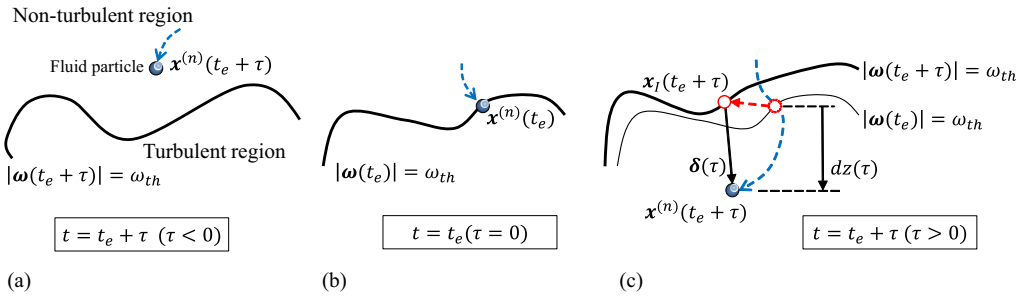

FIG. 10. Lagrangian analysis of turbulent entrainment across the TNTI. (a) Fluid particles are released in nonturbulent regions near the interface. (b) The time τ is defined for each particle as the elapse time after the particle crosses the irrotational boundary (enstrophy isosurface). The particle is located on the irrotational boundary at $t = t_e$. Lagrangian statistics are calculated as a function of τ. (c) A marker of enstrophy isosurface is placed at $\boldsymbol{x}^{(n)}(t_e)$, and then is tracked with the velocity of enstrophy isosurface movement. The location of the particle relative to the irrotational boundary is defined as the separation vector $\boldsymbol{\delta}(\tau)$. The figure also shows the vertical distance $dz(\tau) = z^{(n)}(t_e+\tau) - z^{(n)}(t_e)$ from the location where the fluid particle enters the turbulent region.

three particles of the tetrahedron are placed at $\boldsymbol{x}_2 = \boldsymbol{x}_0 + r_0\boldsymbol{e}_x$, $\boldsymbol{x}_3 = \boldsymbol{x}_0 + r_0\boldsymbol{e}_y$, $\boldsymbol{x}_4 = \boldsymbol{x}_0 + r_0\boldsymbol{e}_z$ ($\boldsymbol{x}_4 = \boldsymbol{x}_0 - r_0\boldsymbol{e}_z$ is used when $z_0 < 0$ so that $\boldsymbol{x}_4$ is in the nonturbulent region), where $\boldsymbol{e}_i$ is the unit vector in the i direction. Here, all particles of the tetrahedra are placed in the nonturbulent region. Then $4 \times 40\,000$ particles are tracked with a third-order Runge-Kutta method and a second-order trilinear interpolation scheme as in previous Lagrangian studies [42,53]. The DNS with the tracking of fluid particles are performed for the release times of the tetrahedra of $t_0 = 130$, 170, and 230 for the case Re20Ri06 and $t_0 = 170$ for the other cases. We consider the tetrahedra with the initial sidelength $r_0 = 2\eta$, 4η, 8η, and 16η. After the particles are released, the DNS are proceeded until $t = t_0 + 90$.

In addition to tracking fluid particles, we introduce markers moving along the irrotational boundary, which are tracked with the velocity of enstrophy isosurface $\boldsymbol{u}_I$, following a DNS study of the entrainment in free shear flows [16]. The normal distance between the entrained particle and the enstrophy isosurface has been also used in previous studies [15]. We use the approach based on the tracking of the enstrophy isosurface; this is because the enstrophy isosurface location closest to the particle can be irrelevant in determining the enstrophy isosurface where the particle will pass during the entrainment after moving for a long time interval. Both approaches are expected to give a similar result for short tracking times $\sim\tau_\eta$ because the entrained particle moves in the direction normal to the enstrophy isosurface in the very early stage of the entrainment [16,26].

Figure 10 shows the Lagrangian analysis performed in this study, where we assume that particle n at $\boldsymbol{x}^{(n)}(t)$ crosses the irrotational boundary at time $t = t_e$. The time elapsed after t_e is denoted by τ. The marker of the enstrophy isosurface, whose location is denoted by $\boldsymbol{x}_I^{(n)}$, is introduced at $\boldsymbol{x}^{(n)}(t_e)$ at time $t = t_e$. The velocity of the enstrophy isosurface movement $\boldsymbol{u}_I$ is represented by the sum of the fluid velocity at $\boldsymbol{x}_I^{(n)}$ and the propagation velocity of the enstrophy isosurface [13] $\boldsymbol{u}_P = u_P\boldsymbol{n}$, where $\boldsymbol{n} = -\nabla\omega^2/|\nabla\omega^2|$ and $u_P = (D\omega^2/Dt)/|\nabla\omega^2|$. This marker at the irrotational boundary $\boldsymbol{x}_I^{(n)}$ is used as a pair with a fluid particle $\boldsymbol{x}^{(n)}$. The entrainment of the fluid particles is studied with $dz(\tau) = z^{(n)}(t_e+\tau) - z^{(n)}(t_e)$ in Fig. 10(c), which is the vertical distance from the location where the particle has crossed the irrotational boundary. With the marker of the irrotational boundary, we can define the relative location between the particle and the irrotational boundary as $\boldsymbol{\delta}(\tau) = \boldsymbol{x}^{(n)}(t_e+\tau) - \boldsymbol{x}_I^{(n)}(t_e+\tau)$. The latter definition of the entrained particle location is more useful for examining the particle location within the TNTI layer than $dz(\tau)$ because both the propagation velocity and the convective fluid motion significantly change the interface location [16,54]. The temporal development of $\boldsymbol{\delta}$ is described by the velocity of the entrained fluid relative to the velocity

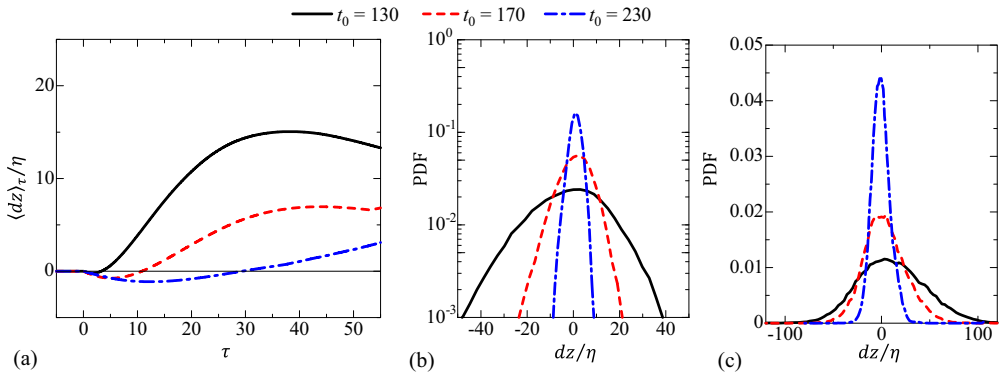

FIG. 11. (a) Averaged vertical distance dz of entrained particles from the irrotational boundary location where the particle has crossed. PDFs of dz/η at (b) $\tau = 6$ and (c) $\tau = 22$. The results are shown for Re20Ri06.

of the irrotational boundary motion, and written as $\delta \boldsymbol{u} = \boldsymbol{u} - \boldsymbol{u}_I$. $\delta \boldsymbol{u}$ can be related to the entrainment velocity across the TNTI layer [16,26] while a positive value of u_P represents the speed at which nonturbulent fluid enters the viscous superlayer passing through the irrotational boundary.

One-particle statistics are calculated from $4 \times 40\,000$ particles as a function of τ [41]. Similarly, the four-particle statistics are calculated as a function of time τ elapsed after one of the particles making up a tetrahedron crosses the irrotational boundary [42]. The average calculated as a function of τ is denoted by $\langle\ \rangle_\tau$. The statistics are calculated for the particles entrained from the upper TNTI. Similar to the Eulerian statistics, the particles entrained from the lower interface are also used for calculating statistics by changing the sign of relevant variables.

B. Location of the entrained particles

Figure 11(a) shows the mean vertical height $\langle dz \rangle_\tau$ normalized by η, where η is taken on the centerline at $t = t_0$. The movement of the entrained fluid particle strongly depends on the release time of the particles. For $t_0 = 130$, the mean vertical location reaches approximately 15η inside the location $z^{(n)}(t_e)$, at which point the particle enters the turbulent core region. $\langle dz \rangle_\tau$ is small for the particles released at later times, and the particles released at $t_0 = 230$, on average, stay close to $z^{(n)}(t_e)$. Figures 11(b) and 11(c) show the PDFs of dz/η at $\tau = 6$ and 22. Although the mean motion of the particles is outward, resulting in $\langle dz \rangle_\tau < 0$ for very small τ, both inward and outward motions occur as confirmed from the PDF in (b). The PDFs for $t_0 = 130$ and 170 in Fig. 11(c) are large for positive dz, and the particles tend to move inward. For $t_0 = 230$, the PDF in Figs. 11(b) and 11(c) has a large peak at $dz \approx 0$, and the particles stay around the vertical height at which they are entrained into the turbulent region.

Since the TNTI propagates and is also convected by the fluid motion, the particle height dz does not correspond to the particle location in relation to the interface location. The particle location within the TNTI layer can be examined with the relative location between the entrained particle and the marker of the irrotational boundary $\boldsymbol{\delta} = (\delta_x, \delta_y, \delta_z)$, where δ_i is the i-direction component of $\boldsymbol{\delta}$. The relative location $\boldsymbol{\delta}$ can be decomposed into the vertical relative distance $\delta_V = \delta_z$ and the horizontal one $\delta_H = \sqrt{\delta_x^2 + \delta_y^2}$. Figures 12(a) and 12(b) show $\langle \delta_H \rangle_\tau / \eta$ and $\langle \delta_V \rangle_\tau / \eta$, respectively. From the case Re20Ri06, it is found that as t_0 increases the particles stay closer to the irrotational boundary location. For $t_0 = 230$, $\langle \delta_H \rangle_\tau$ and $\langle \delta_V \rangle_\tau$ are approximately 5η even at $\tau = 50$, and the entrained particles stay within the TNTI layer, where the vorticity magnitude is smaller than in the turbulent core region (Fig. 4). The particles entrained at earlier time are able to penetrate into the turbulent core region as evidenced by the rapid increases of $\langle \delta_H \rangle_\tau$ and $\langle \delta_V \rangle_\tau$. The insets shows $\langle \delta_H \rangle_\tau / \eta$ and $\langle \delta_V \rangle_\tau / \eta$ against τ normalized by the Kolmogorov timescale $\tilde{\tau}_\eta = (\nu / \langle \tilde{\varepsilon} \rangle)^{1/2}$, where both η and τ_η are taken at $t = t_0$ on the centerline. The plots with the normalization by the dissipative scales collapse

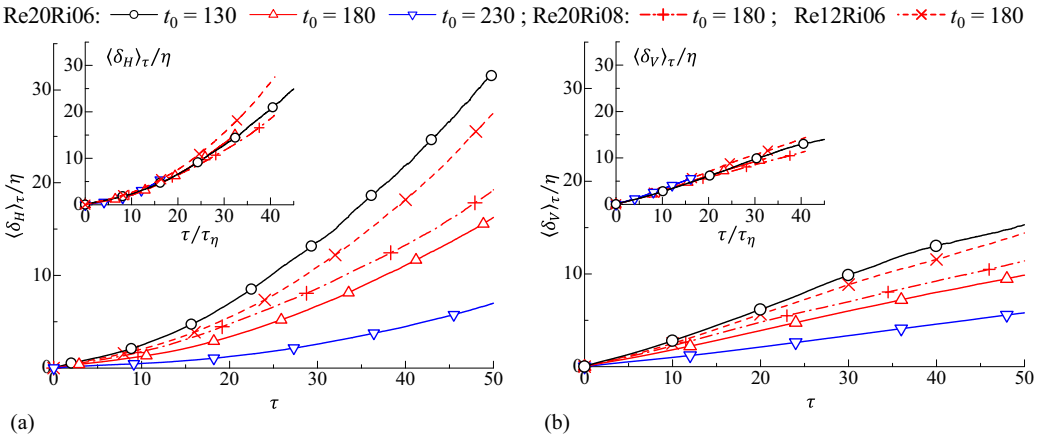

FIG. 12. The mean distance between the entrained particle and the irrotational boundary location. (a) Horizontal distance. (b) Vertical distance. The insets show the distance normalized by the Kolmogorov lengthscale against time normalized by the Kolmogorov timescale. The figure shows the results for $\tau \leqslant 50$. The results from all DNS cases are plotted in these figures.

onto a single curve, especially for small τ. This is because the speed at which the entrained fluid enter the viscous superlayer is given by u_P, which is dominated by the viscous effects as shown in Fig. 9(a). This viscous scaling of u_P has been also found in nonstratified mixing layers [26,50] and in other flows [13–15,27,29]. The collapse with the viscous scales indicates that the entrained particle location in relation to the TNTI is dominated by the small-scale motions of turbulence in the mixing layer. Therefore buoyancy only indirectly affects the entrained fluid motions within the TNTI layer; the rapid decay of ε is due to buoyancy; however, the initial movement of the entrained fluid still scales only with ε and ν.

C. Density on the entrained particle path

Figure 13(a) shows the mean density $\langle \rho' \rangle_\tau$ on the entrained particle path. Note that the statistics are presented for the particles entrained from the lower-density (upper) side of the mixing layer. The density at the fluid particle location increases as the particles are entrained. It should be noticed that, for particles released at later times, especially for $t_0 = 230$, the density hardly changes during the

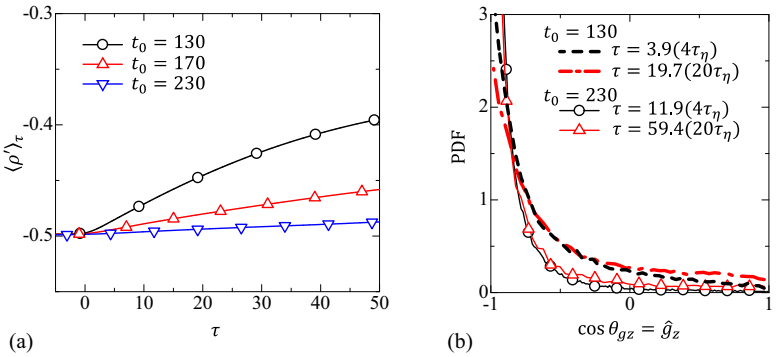

FIG. 13. Lagrangian statistics of density during the entrainment in Re20Ri06. (a) Mean density. (b) PDFs of the vertical component of normalized density gradient $n_{\rho z} = \boldsymbol{n}_\rho \cdot \boldsymbol{e}_z$ near the TNTI.

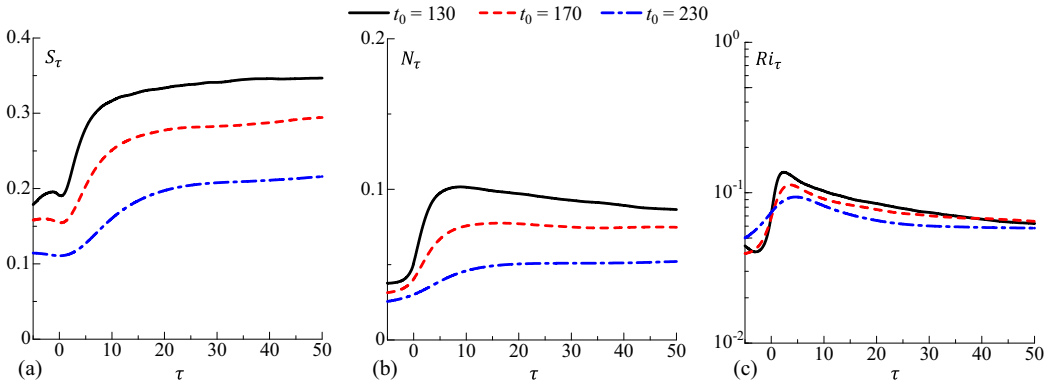

FIG. 14. (a) Mean vertical shear S_τ ($\tilde{S}_\tau = \langle \partial \tilde{u}/\partial \tilde{z} \rangle_\tau$) and (b) buoyancy frequency N_τ ($\tilde{N}_\tau = \sqrt{-(g/\rho_0)\langle \partial \tilde{\rho}/\partial \tilde{z} \rangle_\tau}$) on the entrained particle path in Re20Ri06. (c) The local Richardson number for the entrained particles $\mathrm{Ri}_\tau = N_\tau^2/S_\tau^2$ in Re20Ri06.

entrainment. As confirmed from the particle locations in Fig. 12, these entrained particles with lower density remain outside the more turbulent region where the average density is higher. Figure 13(b) shows the PDF of the vertical component of normalized density gradient $n_{\rho z} = \boldsymbol{n}_\rho \cdot \boldsymbol{e}_z$ measured on the Lagrangian particle path for particles released at $t_0 = 130$ and 230. Overturning motions with $n_{\rho z} > 0$ can be found more frequently during entrainment for particles released at $t_0 = 130$, while overturning is almost absent for particles entrained at later times. These statistics indicate that the fluid entrained at later times remains above the turbulent region, creating a stably stratified layer near the outer edge of the turbulent region.

The buoyancy frequency along the entrained particle path can be defined by N_τ (in dimensional form, $\tilde{N}_\tau = \sqrt{-(g/\rho_0)\langle \partial \tilde{\rho}/\partial \tilde{z} \rangle_\tau}$). Similarly, the mean vertical shear is $S_\tau = \langle \partial u/\partial z \rangle_\tau$ (in dimensional form $\tilde{S}_\tau = \langle \partial \tilde{u}/\partial \tilde{z} \rangle_\tau$). Then, the local Richardson number is defined as $\mathrm{Ri}_\tau = N_\tau^2/S_\tau^2$ ($= \tilde{N}_\tau^2/\tilde{S}_\tau^2$). These are plotted in Fig. 14, whereas the Eulerian counterparts were shown in Fig. 7. The mean vertical shear S_τ acting at the entrained particle location rapidly increases once the particle enters the turbulent region. Similarly, the buoyancy frequency N_τ also increases as the particles are entrained. However, the buoyancy frequency on the entrained particle path, N_τ, is much smaller than the Eulerian one, which reaches a peak within the TNTI layer, while the vertical shear S_τ is higher. Because of small N_τ and high S_τ, the local Richardson number on the entrained particle path is also small compared with Ri_I computed in an Eulerian frame, as confirmed from a comparison between Figs. 7(c) and 14(c). Thus, although there is a region with large Richardson number within the TNTI layer, the particles being entrained within the TNTI layer tend to circumvent this region and to pass into the region with small Richardson number.

D. Vorticity evolution on the entrained particle path

The mean vorticity magnitude for the entrained particles is shown in Fig. 15(a). Once a particle enters the turbulent region, its vorticity begins to grow rapidly. A much slower growth rate, however, is observed for about $\tau > 15$. Even for large τ, the Lagrangian mean vorticity magnitude is smaller than the Eulerian counterpart, as found by comparing Figs. 4(a) and 15(a). The slow growth of the enstrophy on the Lagrangian path is also related to the turbulence decay. Even at the same time, however, $\langle |\boldsymbol{\omega}| \rangle_\tau$ is smaller than $\langle |\boldsymbol{\omega}| \rangle_I$ in the turbulent core region. For example, we can see that $\langle |\boldsymbol{\omega}| \rangle_\tau = 0.35$ at $\tau = 40$ for $t_0 = 130$ (i.e., $t = 170$) and $\langle |\boldsymbol{\omega}| \rangle_I = 0.46$ in the turbulent core region ($\zeta_I/\eta = -50$) at $t = 170$. The particles entrained at later times stay longer within the TNTI layer (Fig. 12), where the vorticity magnitude is smaller than in the turbulent core region. Additionally, the mean vorticity calculated in an Eulerian frame in Fig. 4(a) includes a contribution

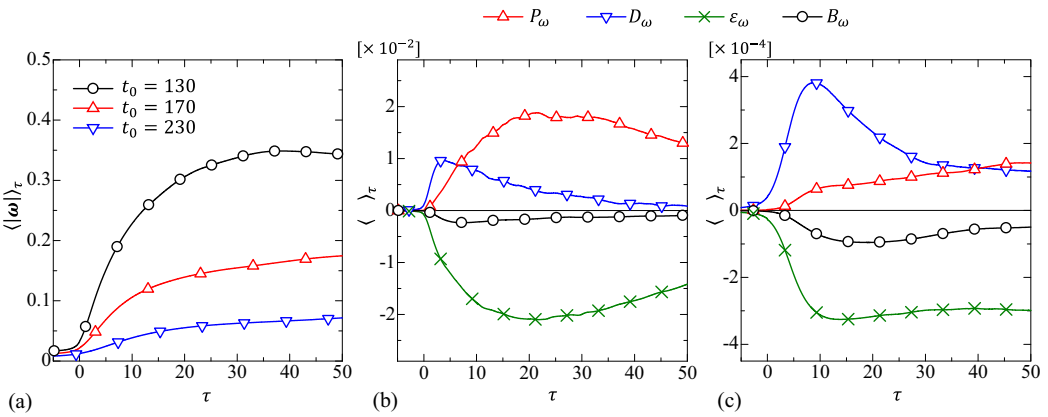

FIG. 15. Lagrangian statistics of vorticity evolution during the entrainment in Re20Ri06. (a) Conditional mean vorticity magnitude. Averaged enstrophy transport equation for the particles released at (b) $t_0 = 130$ and (c) $t_0 = 230$.

from fluids existing in the turbulent region, whose characteristics are different from the fluids being entrained [16]. Therefore, it takes very long time for entrained particles to gain vorticity comparable to that of the fluid existing in the turbulent core region.

Figures 15(b) and 15(c) show terms in the averaged enstrophy equation [Eq. (12)] for the entrained particles released at $t_0 = 130$ and 230, respectively. The enstrophy evolution near the TNTI in an Eulerian frame can be found for the stratified mixing layers in Fig. 9(a) and in Ref. [31], and for gravity currents in Ref. [29]. We can observe qualitative differences in the enstrophy evolution between the Eulerian and Lagrangian statistics. In the Eulerian statistics in stratified mixing layers in [31], the averaged enstrophy production term in the turbulent core region is much larger than the averaged viscous diffusion term near the TNTI. Although the enstrophy production term averaged in a Lagrangian frame becomes important for large τ, the maximum value of $\langle P_\omega \rangle_\tau$, found at $\tau \approx 20$, is comparable to the viscous diffusion term at the initial stage of the entrainment, $\tau \approx 3$. This difference indicates that inviscid vortex stretching is less efficient for fluids being entrained than for fluids existing in the turbulent region. For a particle entrained at the later time $t_0 = 230$, the mean enstrophy growth due to enstrophy production is comparable to the growth due to viscous diffusion, even for large τ. Furthermore, $\langle D_\omega \rangle_\tau$ does not approach 0 with time, implying that the viscous effects keep transferring the vorticity from the turbulent fluid with larger $\omega^2/2$ to the fluid being entrained. This is related to the fact that particles entrained at later times hardly penetrate to the turbulent core region, but remain close to the outer edge of the TNTI layer. It is also found that, unlike Eulerian statistics found in stratified mixing layers [31] and gravity currents [29], the baroclinic torque B_ω has an important contribution to the vorticity dynamics of the entrained fluids.

Figure 16 shows the PDF of each term in Eq. (12) at $\tau = 4\tau_\eta$ and $\tau = 20\tau_\eta$ for the release times $t_0 = 130$ and 230. While the baroclinic torque is small compared with the other terms for $t_0 = 130$ [Figs. 16(a) and 16(b)], it becomes as important as the other terms for particles entrained at the later time [Figs. 16(c) and 16(d)]. For $t_0 = 230$, the PDF of B_ω is negatively skewed, indicating that the baroclinic torque reduces the enstrophy, and slows the enstrophy growth of the entrained fluid. It is also found that P_ω and D_ω have a comparable effect on the enstrophy growth at $\tau = 20\tau_\eta$, while P_ω becomes more important than D_ω in the nonstratified free shear flows once the entrained particle reaches the turbulent sublayer [16].

Figure 17 shows the PDF of the second invariant of the velocity gradient tensor $Q = (\omega_i\omega_i - 2S_{ij}S_{ij})/4$ obtained both as Eulerian [Figs. 17(a) and 17(b)] and as Lagrangian [Figs. 17(c) and 17(d)] statistics. From the Eulerian PDF, we can find that in most of the regions at $\zeta_I/\eta = -2$ the strain-rate dominates over the vorticity ($Q < 0$). Apart from the outer edge of the TNTI layer ($\zeta_I/\eta = -6, -9$,

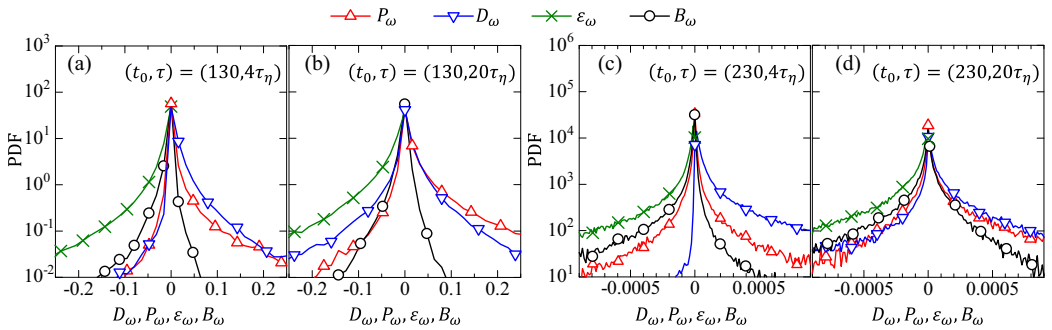

FIG. 16. PDFs of enstrophy transport equation calculated from the Lagrangian particles released at (a, b) $t_0 = 130$ and (c, d) $t_0 = 230$ in Re20Ri06. (a,c) $\tau = 4\tau_\eta$, (b,d) $\tau = 20\tau_\eta$.

and -18), a vorticity dominant region ($Q > 0$) also appears in the Eulerian PDF, as shown in Figs. 17(a) and 17(b). However, the PDF obtained on the entrained particle path is negatively skewed as, in the entrained particle path, the strain-rate dominates the vorticity ($Q < 0$). Thus, the region with strong vorticity ($Q \gg 0$) near the TNTI mostly consists of fluid which has been existing in the turbulent region rather than the fluid being entrained from the nonturbulent regions, and the fluid being entrained within the TNTI layer tends to circumvent the region with strong vorticity.

E. Four-particle statistics: Material volume evolution during the entrainment

Four-particle statistics are presented for investigating material volume evolution during entrainment. We consider four-particle clusters (tetrahedra) with the initial side length r_0 equal to 2η, 4η, 8η, or 16η entrained from nonturbulent regions. The location and velocity of the particles are given by $\boldsymbol{x}^{(n)}$ and $\boldsymbol{u}^{(n)}$, where $n = 1,...,4$. The center of the four particles is defined as $\overline{\boldsymbol{x}} = \sum_{n=1}^{4} \boldsymbol{x}^{(n)}/4$, where the overbar denotes the average over the four particles. The particle location relative to $\overline{\boldsymbol{x}}$ is given by $\boldsymbol{r}^{(n)} = \boldsymbol{x}^{(n)} - \overline{\boldsymbol{x}}$. The velocity of the four particles' center is $\overline{\boldsymbol{u}}$ while the particle velocity relative to $\overline{\boldsymbol{u}}$ is $\boldsymbol{u}'^{(n)} = \boldsymbol{u}^{(n)} - \overline{\boldsymbol{u}}$.

The kinetic energies of the mean and relative motions of tetrahedra are defined as $E_m = \overline{\boldsymbol{u}} \cdot \overline{\boldsymbol{u}}/2$ and $E_r = \overline{\boldsymbol{u}' \cdot \boldsymbol{u}'}/2$, respectively. For the tetrahedra with $E_m \gg E_r$, the four particles move mainly along with the four particles' center. Figures 18(a) and 18(b) show the evolution of $\langle E_m \rangle_\tau$ and $\langle E_r \rangle_\tau$ during the entrainment of the particles released at $t_0 = 130$ and 230. For $t_0 = 130$, $\langle E_m \rangle_\tau$ slightly

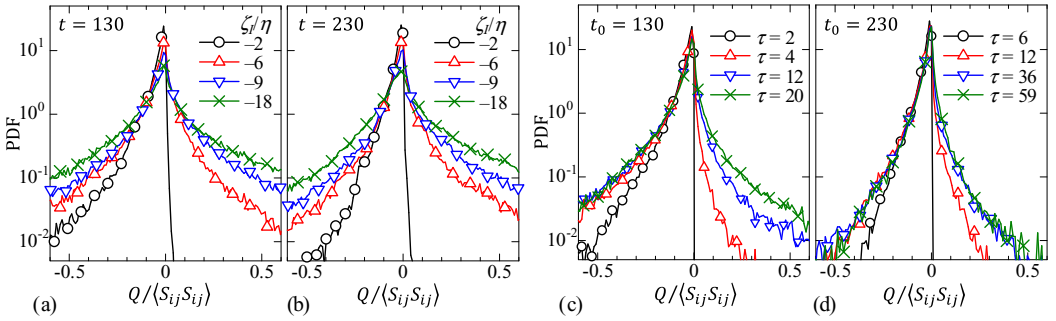

FIG. 17. Comparison between (a, b) Eulerian and (c, d) Lagrangian PDFs of the second invariant of velocity gradient tensor Q in Re20Ri06. The Eulerian PDFs are calculated at (a) $t = 130$ and (b) $t = 230$ while the Lagrangian PDFs are calculated with the particles released at (c) $t_0 = 130$ and (d) $t_0 = 230$. The PDFs are normalized by the mean strain-product $\langle S_{ij} S_{ij} \rangle$ on the centerline.

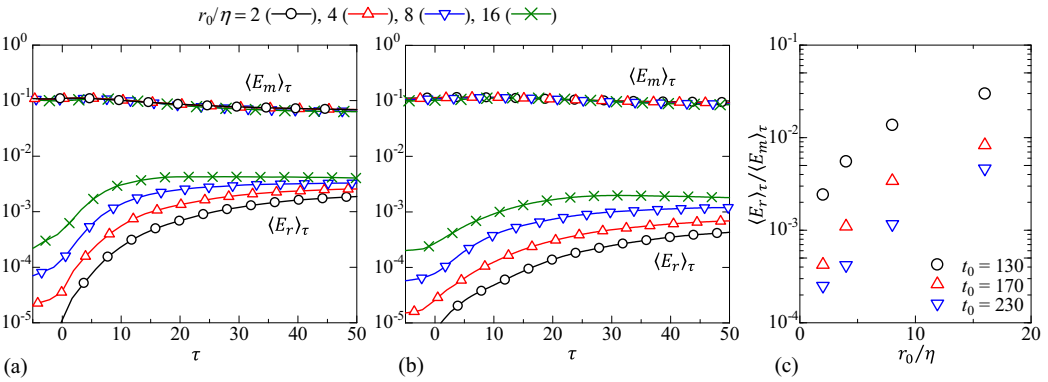

FIG. 18. Averaged kinetic energies in mean (E_m) and relative (E_r) motions of the tetrahedra with the initial size of $r_0/\eta = 2$, 4, 8, and 16 released at (a) $t_0 = 130$ and (b) $t_0 = 230$. (c) The ratio between the averaged kinetic energies in mean and relative motions. The results are shown for Re20Ri06.

decreases after the particles are entrained because of the behavior of the mean streamwise velocity, as depicted by its vertical profile. However, for $t_0 = 230$, the energy of the motion of the center of the tetrahedra hardly changes during the entrainment, since $\langle E_m \rangle_\tau \approx 0.1$ even for large τ. The mean motion hardly changes during the entrainment while the tetrahedra in the nonturbulent region are convected by the horizontal mean flow. This horizontal convective motion dominates the motion of the center even after they are entrained into the turbulent region for $t_0 = 230$. For both t_0, the relative motion ($\langle E_r \rangle_\tau$) rapidly grows during the entrainment process ($\tau > 0$), as the particles begin to become separated as they are entrained. This separation often causes the deformation of the fluid volumes. It is clear in the figure that the larger tetrahedra gain more energy in the relative motion. However, $\langle E_r \rangle_\tau$ for the particles entrained at the later time $t_0 = 230$ is much smaller than at $t_0 = 130$. These dependencies of $\langle E_r \rangle_\tau$ on t_0 and r_0 are also confirmed in Fig. 18(c), where the ratio between the energies in mean and relative motions at $\tau = 10$ is plotted as a function of r_0/η. This ratio is smaller for earlier times t_0, and is significantly lower for $r_0/\eta < 10$, especially for smaller r_0/η, indicating that a fluid volume smaller than $\sim 10\eta$ is entrained along with the center-of-mass motion.

With horizontal and vertical velocities defined by $\boldsymbol{u}_H$ and $\boldsymbol{u}_V$, respectively, the kinetic energies E_m and E_r can be decomposed into the horizontal and vertical components $E_m = E_{mH} + E_{mV}$ and $E_r = E_{rH} + E_{rV}$, where $E_{mH} = \overline{\boldsymbol{u}_H} \cdot \overline{\boldsymbol{u}_H}/2$, $E_{mV} = \overline{\boldsymbol{u}_V} \cdot \overline{\boldsymbol{u}_V}/2$, $E_{rH} = \overline{\boldsymbol{u}'_H \cdot \boldsymbol{u}'_H}/2$, and $E_{rV} = \overline{\boldsymbol{u}'_V \cdot \boldsymbol{u}'_V}/2$. The evolution of E_{mH}, E_{mV}, E_{rH}, and E_{rV} is shown in Fig. 19(a) for the tetrahedra with $r_0 = 4\eta$ released at $t_0 = 170$. It is found that the mean motion of tetrahedra is dominated by the horizontal velocity. The decomposition of the kinetic energy into the mean and relative motions is related to the scale decomposition [55], where E_m and E_r are the energies in large and small scales, respectively, and the length scale which characterizes this decomposition is the size of the tetrahedron. Therefore, a small value of E_{mV} is due to the horizontal mean flow and the buoyancy effects on the large-scale motions, by which large-scale vertical motions are suppressed. The horizontal relative motion E_{rH} grows more rapidly than in the corresponding vertical one, and, during entrainment, the four particles tend to separate in the horizontal direction. The dependence on t_0 can be found in Fig. 19(b), where the ratio between the horizontal and vertical motions, $\langle E_{mV} \rangle_\tau / \langle E_{mH} \rangle_\tau$ and $\langle E_{rV} \rangle_\tau / \langle E_{rH} \rangle_\tau$, are plotted for the tetrahedra with $r_0 = 4\eta$. The tetrahedra entrained at later times possess less kinetic energy in the vertical direction, and this tendency is clearer in the relative motion. This is because the Ozmidov scale decreases with time and the energy in smaller scales related to the relative motion is suppressed by buoyancy at later times. A small value of $\langle E_{rV} \rangle_\tau / \langle E_{rH} \rangle_\tau$ shows that the four-particle clusters entrained at later times are hardly separated in the vertical direction, although they can be diffused in the horizontal direction. A horizontal layer of entrained fluid can be

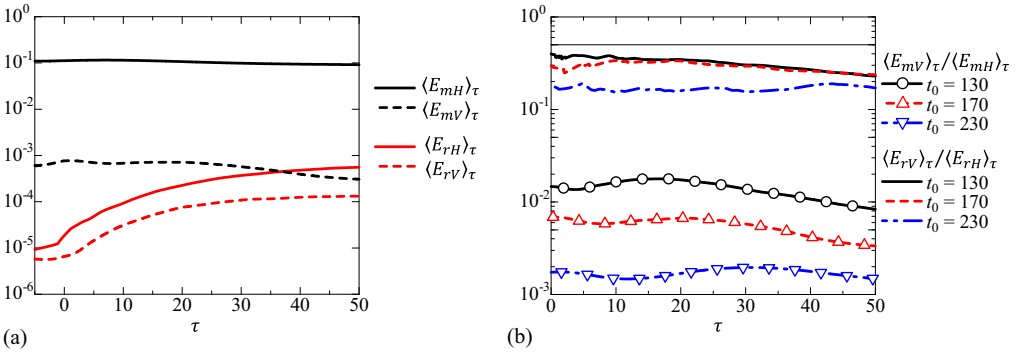

FIG. 19. (a) Comparison of averaged kinetic energies in mean and relative motions of the tetrahedra between the horizontal (E_{mH}, E_{rH}) and vertical components (E_{mV}, E_{rV}) calculated from the tetrahedra with $r_0 = 4\eta$ released at $t_0 = 170$. (b) The ratio between the horizontal and vertical components of averaged kinetic energies in mean and relative motions. The results are shown for Re20Ri06.

formed over the fluid existing in the turbulent region without mixing with the fluid in the turbulent core region.

The growth of the kinetic energy of the relative motion results from the deformation of the tetrahedra. The shape and volume of a tetrahedron are characterized by the volumetric tensor [56] defined by $R_{ij} = \overline{r_i r_j}$, which has three eigenvalues denoted by R_a, R_b, and R_c ($R_a \geqslant R_b \geqslant R_c$). The corresponding eigenvectors are $\boldsymbol{a}$, $\boldsymbol{b}$, and $\boldsymbol{c}$. The shape of the tetrahedra is characterized by two parameters [56]: elongation $E = 1 - \sqrt{R_b/R_a}$ and planarity $P = 1 - \sqrt{R_c/R_b}$. $\boldsymbol{a}$ and $\boldsymbol{c}$ represent the directions of the elongation and the planarity normal respectively. A tetrahedron with $P \approx 1$ has a flatten shape with four particles nearly on a plane while $E \approx 1$ when four particles lie nearly on a straight line. Figure 20 shows the mean evolution of E and P for the tetrahedra with $r_0 = 4\eta$. The shape starts to change once the particles enter the TNTI layer, as the tetrahedra approach elongated and flatten shapes. The deformation of the tetrahedra is related to the energy cascade process [57,58]. The deformation during the entrainment indicates that nonlinearity becomes important once the tetrahedra enter the turbulent region. The rate of deformation depends on the release time of the particles, as the tetrahedra entrained at earlier times deform more rapidly. It was shown that the deformation rates of small tetrahedra are characterized by the Kolmogorov timescale $(\nu\langle\tilde{\varepsilon}\rangle)^{1/2}$ [42]. Therefore, the rapid decay of ε due to buoyancy effects can be related to the observed t_0-dependence of the deformation rate.

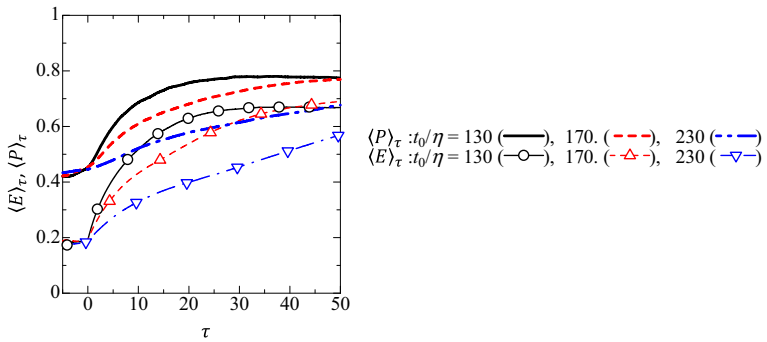

FIG. 20. The averaged shape evolution of tetrahedra with $r_0 = 4\eta$ in Re20Ri06, where the shape is characterized by elongation E and planarity P defined with the eigenvalues of the volumetric tensor [56].

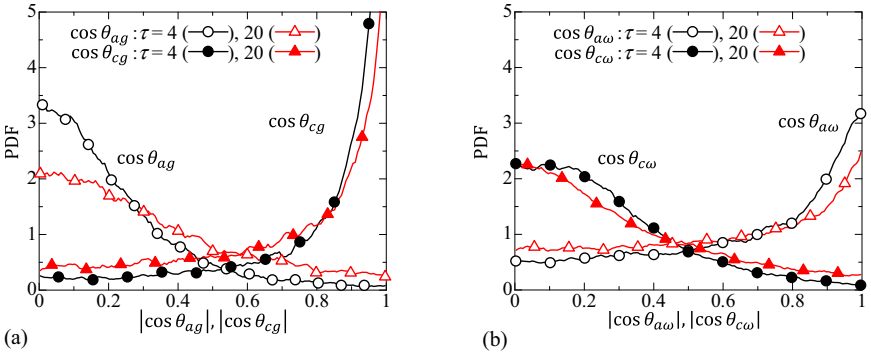

FIG. 21. Alignment statistics among the elongation and planarity-normal directions ($\boldsymbol{a}$, $\boldsymbol{c}$) of tetrahedra, the density gradient ($\hat{\boldsymbol{g}} = \boldsymbol{g}/|\boldsymbol{g}|$), and the vorticity vector ($\hat{\boldsymbol{\omega}} = \boldsymbol{\omega}/|\boldsymbol{\omega}|$) for the tetrahedra with $r_0/\eta = 4$ released at $t_0 = 170$. (a) PDF of $|\cos\theta_{ag}| = |\boldsymbol{a} \cdot \hat{\boldsymbol{g}}|$ and $|\cos\theta_{cg}| = |\boldsymbol{c} \cdot \hat{\boldsymbol{g}}|$. (b) PDF of $|\cos\theta_{a\omega}| = |\boldsymbol{a} \cdot \hat{\boldsymbol{\omega}}|$ and $|\cos\theta_{c\omega}| = |\boldsymbol{c} \cdot \hat{\boldsymbol{\omega}}|$.

Figure 21 shows the alignment characteristics of the vorticity vector $\boldsymbol{\omega}$, the density gradient $\boldsymbol{g}$, and the elongation and planarity-normal directions ($\boldsymbol{a}$ and $\boldsymbol{c}$). The PDFs show that the planarity normal $\boldsymbol{c}$ tends to align with the local density gradient ($|\boldsymbol{c} \cdot \hat{\boldsymbol{g}}| \approx 1$) while the direction of the elongation given by $\boldsymbol{a}$ tends to align with the vorticity direction ($|\boldsymbol{a} \cdot \hat{\boldsymbol{\omega}}| \approx 1$), in agreement with the results for nonstratified flows [42]. In stratified mixing layers, buoyancy effects cause the density gradient to point in the vertical direction, and therefore, the entrained tetrahedra are flattened in the vertical direction during entrainment. This shape evolution is related to larger kinetic energy in the relative horizontal motion than in the vertical motion, and thus the entrained fluid volume is diffused mostly in the horizontal direction, without penetrating into the turbulent core region, especially after the mixing layer begins to become layered.

V. CONCLUDING REMARKS

Using direct numerical simulation, the entrainment process in a temporally-evolving stably-stratified mixing layer is investigated in relation to the TNTI defined in terms of the vorticity field. The buoyancy Reynolds number Re_b at an initial stage of the decay is large enough for small scale turbulence to exist in the stratified mixing layer. Re_b decreases with time due to the rapid decay of the kinetic energy dissipation rate; this results in the layering of the flow without significant small-scale fluctuations. The statistics in Eulerian and Lagrangian frames are presented for these different stages of the decay.

The mean vorticity profile near the TNTI confirms that the thickness of the TNTI is approximately 12η, even after the flow begins to become layered, consistent with nonstratified flows and stratified flows at higher Re_b. The overturning motions are more frequently observed in the turbulent core region than within the TNTI layer because Re_b is small near the interface, even if the turbulent core region has higher Re_b. Once the flow begins to become layered, the overturns are absent near the TNTI.

The entrained fluid movement in relation to the TNTI layer is dominated by the small dissipative scales. Therefore, the rapid decay of ε due to buoyancy causes the entrained particle movement to become slow in relation to the interface. Once the layered structures with small ε form, the entrained particles remain within the TNTI layer over a long period of time. In contrast, particles are able to penetrate into the turbulent core region when Re_b is large enough for small-scale turbulence to exist in the turbulent regions.

The change in the flow structures affects the vorticity dynamics near the TNTI layer except for the viscous superlayer, where viscous diffusion dominates the vorticity growth. When small-scale

turbulence exists, inviscid vortex stretching dominates the enstrophy evolution within the turbulent sublayer [31]. However, once the flow begins to become layered, the baroclinic torque, which tends to reduce the enstrophy, becomes important. Furthermore, the baroclinic torque has a stronger influence for fluid being entrained than for the existing turbulent fluid, and causes the vorticity growth to become slow during entrainment. There exists turbulent fluid with strong vorticity or with large buoyancy frequency near the TNTI. However, the particles being entrained within the TNTI layer circumvent these regions, and they pass through the TNTI in the strain-dominant regions or the regions with small buoyancy frequency.

Multiparticle statistics are used for investigating the fluid volume evolution during entrainment. The entrainment causes the increase of the kinetic energy in the horizontal motion relative to the tetrahedral particles' center, and the fluid volume is diffused in the horizontal direction. This horizontal relative motion causes the entrained fluid volumes to deform and to be flattened in the density gradient direction, which mostly aligns with the vertical direction. Once the layer structures begin to be formed, the entrained fluid volumes hardly penetrate into the turbulent core region because of the suppression of vertical motion. Therefore, the entrained fluid volume remains near the outer edge of the turbulent region and forms a stably stratified layer without significant vertical overturning motions.

ACKNOWLEDGMENTS

The numerical simulations presented in this manuscript were carried out on the high performance computing system (NEC SX-ACE) in the Japan Agency for Marine-Earth Science and Technology. This work was partially supported by "Collaborative Research Project on Computer Science with High-Performance Computing in Nagoya University," by MEXT KAKENHI Grants No. 16K18013 and No. 25289030, and by the U.S. Office of Naval Research via Grant No. N00014-15-1-2248.

[1] L. Mahrt, Stably stratified atmospheric boundary layers, Annu. Rev. Fluid Mech. **46**, 23 (2014).
[2] S. A. Thorpe, The near-surface ocean mixing layer in stable heating conditions, J. Geophys. Res. **83**, 2875 (1978).
[3] C. B. da Silva, J. C. R. Hunt, I. Eames, and J. Westerweel, Interfacial layers between regions of different turbulence intensity, Annu. Rev. Fluid Mech. **46**, 567 (2014).
[4] S. Corrsin and A. L. Kistler, Free-stream boundaries of turbulent flows, NACA Technical Report No. TN-1244 (1955).
[5] S. A. Thorpe, Recent developments in the study of ocean turbulence, Annu. Rev. Earth Planet. Sci. **32**, 91 (2004).
[6] T. H. Ellison and J. S. Turner, Turbulent entrainment in stratified flows, J. Fluid Mech. **6**, 423 (1959).
[7] R. S. Lindzen, Turbulence and stress owing to gravity wave and tidal breakdown, J. Geophys. Res. **86**, 9707 (1981).
[8] L. Mahrt, Stratified atmospheric boundary layers, Boundary-Layer Meteorol. **90**, 375 (1999).
[9] E. J. Strang and H. J. S. Fernando, Entrainment and mixing in stratified shear flows, J. Fluid Mech. **428**, 349 (2001).
[10] E. J. Strang and H. J. S. Fernando, Vertical mixing and transports through a stratified shear layer, J. Phys. Oceanogr. **31**, 2026 (2001).
[11] R. R. Taveira and C. B. da Silva, Characteristics of the viscous superlayer in shear free turbulence and in planar turbulent jets, Phys. Fluids **26**, 021702 (2014).
[12] J. Westerweel, C. Fukushima, J. M. Pedersen, and J. C. R. Hunt, Mechanics of the Turbulent-Nonturbulent Interface of a Jet, Phys. Rev. Lett. **95**, 174501 (2005).

[13] M. Holzner and B. Lüthi, Laminar Superlayer at the Turbulence Boundary, Phys. Rev. Lett. **106**, 134503 (2011).
[14] M. van Reeuwijk and M. Holzner, The turbulence boundary of a temporal jet, J. Fluid Mech. **739**, 254 (2014).
[15] M. Wolf, M. Holzner, B. Lüthi, D. Krug, W. Kinzelbach, and A. Tsinober, Effects of mean shear on the local turbulent entrainment process, J. Fluid Mech. **731**, 95 (2013).
[16] T. Watanabe, C. B. da Silva, Y. Sakai, K. Nagata, and T. Hayase, Lagrangian properties of the entrainment across turbulent/non-turbulent interface layers, Phys. Fluids **28**, 031701 (2016).
[17] M. Holzner, A. Liberzon, N. Nikitin, B. Lüthi, W. Kinzelbach, and A. Tsinober, A Lagrangian investigation of the small-scale features of turbulent entrainment through particle tracking and direct numerical simulation, J. Fluid Mech. **598**, 465 (2008).
[18] K. Chauhan, J. Philip, C. M. de Silva, N. Hutchins, and I. Marusic, The turbulent/non-turbulent interface and entrainment in a boundary layer, J. Fluid Mech. **742**, 119 (2014).
[19] H. Kato and O. M. Phillips, On the penetration of a turbulent layer into stratified fluid, J. Fluid Mech. **37**, 643 (1969).
[20] P. F. Linden, The interaction of a vortex ring with a sharp density interface: A model for turbulent entrainment, J. Fluid Mech. **60**, 467 (1973).
[21] L. H. Kantha, O. M. Phillips, and R. S. Azad, On turbulent entrainment at a stable density interface, J. Fluid Mech. **79**, 753 (1977).
[22] A. B. Cortesi, B. L. Smith, G. Yadigaroglu, and S. Banerjee, Numerical investigation of the entrainment and mixing processes in neutral and stably-stratified mixing layers, Phys. Fluids **11**, 162 (1999).
[23] M. Mory, A model of turbulent mixing across a density interface including the effect of rotation, J. Fluid Mech. **223**, 193 (1991).
[24] D. J. Carruthers and J. C. R. Hunt, Velocity fluctuations near an interface between a turbulent region and a stably stratified layer, J. Fluid Mech. **165**, 475 (1986).
[25] C. B. da Silva and J. C. F. Pereira, Invariants of the velocity-gradient, rate-of-strain, and rate-of-rotation tensors across the turbulent/nonturbulent interface in jets, Phys. Fluids **20**, 055101 (2008).
[26] T. Watanabe, Y. Sakai, K. Nagata, Y. Ito, and T. Hayase, Turbulent mixing of passive scalar near turbulent and nonturbulent interface in mixing layers, Phys. Fluids **27**, 085109 (2015).
[27] T. Watanabe, Y. Sakai, K. Nagata, Y. Ito, and T. Hayase, Enstrophy and passive scalar transport near the turbulent-nonturbulent interface in a turbulent planar jet flow, Phys. Fluids **26**, 105103 (2014).
[28] D. K. Bisset, J. C. R. Hunt, and M. M. Rogers, The turbulent-nonturbulent interface bounding a far wake, J. Fluid Mech. **451**, 383 (2002).
[29] D. Krug, M. Holzner, B. Lüthi, M. Wolf, W. Kinzelbach, and A. Tsinober, The turbulent-nonturbulent interface in an inclined dense gravity current, J. Fluid Mech. **765**, 303 (2015).
[30] T. Watanabe, J. J. Riley, S. M. de Bruyn Kops, P. J. Diamessis, and Q. Zhou, Turbulent-nonturbulent interfaces in wakes in stably stratified fluids, J. Fluid Mech. **797**, R1 (2016).
[31] T. Watanabe, J. J. Riley, and K. Nagata, Effects of stable stratification on turbulent-nonturbulent interfaces in turbulent mixing layers, Phys. Rev. Fluids **1**, 044301 (2016).
[32] D. Krug, D. Chung, J. Philip, and I. Marusic, Global and local aspects of entrainment in temporal plumes, J. Fluid Mech. **812**, 222 (2017).
[33] M. Holzner and M. van Reeuwijk, The turbulent-nonturbulent interface in penetrative convection, J. Turbulence **18**, 260 (2017).
[34] W. D. Smyth and J. N. Moum, Length scales of turbulence in stably stratified mixing layers, Phys. Fluids **12**, 1327 (2000).
[35] I. P. D. De Silva, H. J. S. Fernando, F. Eaton, and D. Hebert, Evolution of Kelvin-Helmholtz billows in nature and laboratory, Earth Planet. Sci. Lett. **143**, 217 (1996).
[36] J. N. Moum, Efficiency of mixing in the main thermocline, J. Geophys. Res. **101**, 12057 (1996).
[37] A. M. Abdilghanie and P. J. Diamessis, The internal gravity wave field emitted by a stably stratified turbulent wake, J. Fluid Mech. **720**, 104 (2013).
[38] W. D. Smyth and J. N. Moum, Anisotropy of turbulence in stably stratified mixing layers, Phys. Fluids **12**, 1343 (2000).

[39] W. D. Smyth, Dissipation-range geometry and scalar spectra in sheared stratified turbulence, J. Fluid Mech. **401**, 209 (1999).
[40] B. D. Mater and S. K. Venayagamoorthy, The quest for an unambiguous parametrization of mixing efficiency in stably stratified geophysical flows, Geophys. Res. Lett. **41**, 4646 (2014).
[41] R. R. Taveira, J. S. Diogo, D. C. Lopes, and C. B. da Silva, Lagrangian statistics across the turbulent-nonturbulent interface in a turbulent plane jet, Phys. Rev. E **88**, 043001 (2013).
[42] T. Watanabe, C. B. da Silva, and K. Nagata, Multiparticle dispersion during entrainment in turbulent free-shear flows, J. Fluid Mech. **805**, R1 (2016).
[43] C. Staquet and J. J. Riley, A numerical study of a stably stratified mixing layer, in *In Selected Papers from the Sixth Symposium on Turbulent Shear Flows* (Springer, Berlin, 1989), pp. 381–397.
[44] K. A. Brucker and S. Sarkar, Evolution of an initially turbulent stratified shear layer, Phys. Fluids **19**, 105105 (2007).
[45] A. Kempf, M. Klein, and J. Janicka, Efficient generation of initial-and inflow-conditions for transient turbulent flows in arbitrary geometries, Flow, Turbul. Combust. **74**, 67 (2005).
[46] Y. Morinishi, T. S. Lund, O. V. Vasilyev, and P. Moin, Fully conservative higher order finite difference schemes for incompressible flow, J. Comput. Phys. **143**, 90 (1998).
[47] H. A. Van der Vorst, Bi-CGSTAB: A fast and smoothly converging variant of Bi-CG for the solution of nonsymmetric linear systems, SIAM J. Sci. Statist. Comput. **13**, 631 (1992).
[48] W. R. Peltier and C. P. Caulfield, Mixing efficiency in stratified shear flows, Annu. Rev. Fluid Mech. **35**, 135 (2003).
[49] R. Jahanbakhshi, N. S. Vaghefi, and C. K. Madnia, Baroclinic vorticity generation near the turbulent/non-turbulent interface in a compressible shear layer, Phys. Fluids **27**, 105105 (2015).
[50] R. Jahanbakhshi and C. K. Madnia, Entrainment in a compressible turbulent shear layer, J. Fluid Mech. **797**, 564 (2016).
[51] H. Xu, N. T. Ouellette, and E. Bodenschatz, Evolution of geometric structures in intense turbulence, New J. Phys. **10**, 013012 (2008).
[52] J. Schumacher, Lagrangian studies in convective turbulence, Phys. Rev. E **79**, 056301 (2009).
[53] Y. Yang, J. Wang, Y. Shi, Z. Xiao, X. T. He, and S. Chen, Acceleration of Passive Tracers in Compressible Turbulent Flow, Phys. Rev. Lett. **110**, 064503 (2013).
[54] J. Philip, I. Bermejo-Moreno, D. Chung, and I. Marusic, Characteristics of the entrainment velocity in a developing wake, in *Proceedings of the Ninth International Symposium on Turbulence and Shear Flow Phenomena (TSFP-9), Melbourne, Australia* (University of Melbourne, 2015), Vol. 3, paper 9C-5.
[55] A. Naso and A. Pumir, Scale dependence of the coarse-grained velocity derivative tensor structure in turbulence, Phys. Rev. E **72**, 056318 (2005).
[56] P. Robert, A. Roux, C. C. Harvey, M. W. Dunlop, P. W. Daly, and K. H. Glassmeier, Tetrahedron geometric factors, in *Analysis Methods for Multi-Spacecraft Data (ISSI Scientific Report)*, edited by G. Paschmann and P. W. Daly (ESA Publications Division, Noordwijk, the Netherlands, 1998), pp. 323–348.
[57] A. Pumir, B. I. Shraiman, and M. Chertkov, The Lagrangian view of energy transfer in turbulent flow, Europhys. Lett. **56**, 379 (2001).
[58] T. Watanabe and K. Nagata, Gradients estimation from random points with volumetric tensor in turbulence, J. Comput. Phys. **350**, 518 (2017).